EXHIBIT 46 (AR K.11)

Using Moored Arrays and Hyperspectral Aerial Imagery to Develop Nutrient Criteria for New Hampshire's Estuaries

A Final Report to

The New Hampshire Estuaries Project

Submitted by

J. Ru Morrison[1]
Thomas K. Gregory[1]
Shachak Pe'eri[2]
William McDowell[3]
Philip Trowbridge[4]

[1]Coastal Observing Center
[2]Center for Coastal Ocean Mapping
[3]Natural Resources Department
University of New Hampshire
Durham, NH
[4]New Hampshire Estuaries Project

September 30, 2008

This project was funded in part by a grant from the New Hampshire Estuaries Project as authorized by the U.S. Environmental Protection Agency's National Estuary Program.

EXHIBIT 46 (AR K.11)

Table of Contents

1 Abstract

Increasing nitrogen concentrations and declining eelgrass beds in Great Bay, NH are clear indicators of impending problems for the state's estuaries. A workgroup established in 2005 by the NH Department of Environmental Services and the NH Estuaries Project (NHEP) adopted eelgrass survival as the water quality target for nutrient criteria development for NH's estuaries. In 2007, the NHEP received a grant from the U.S. Environmental Protection Agency to collect water quality information including that from moored sensors and hyper-spectral imagery data of the Great Bay Estuary. Data from the Great Bay Coastal Buoy, part of the regional Integrated Ocean Observing System (IOOS), were used to derive a multivariate model of water clarity with phytoplankton, Colored Dissolved Organic Matter (CDOM), and non-algal particles. Non-algal particles include both inorganic and organic matter. Most of the temporal variability in the diffuse attenuation coefficient of Photosynthetically Available Radiation (PAR) was associated with non-algal particles. However, on a mean daily basis non-algal particles and CDOM contributed a similar fraction (~30 %) to the attenuation of light. The contribution of phytoplankton was about a third of the other two optically important constituents. CDOM concentrations varied with salinity and magnitude of riverine inputs demonstrating its terrestrial origin. Non-algal particle concentration also varied with river flow but also wind driven resuspension.

Twelve of the NHEP estuarine assessment zones were observed with the hyperspectral aerial imagery on August 29 and October 17. A concurrent in situ effort included buoy measurements, continuous along-track sampling, discrete water grab samples, and vertical profiles of light attenuation. PAR effective attenuation coefficients retrieved from deep water regions in the imagery agreed well with in-situ observations. Water clarity was lower and optically important constituent concentrations were higher in the tributaries. Eelgrass survival depth, estimated as the depth at which 22% of surface light was available, ranged from less than half a meter to over two meters. The best water clarity was found in the Great Bay (GB), Little Bay (LB), and Lower Piscataqua River (LPR) assessment zones. Absence of eelgrass from these zones would indicate controlling factors other than water clarity.

2 Executive Summary

Eelgrass, like all plants, needs light to survive. Light in the visible range of the spectrum from 400 to 700 nm can drive power photosynthesis defining the spectral range of Photosynthetically Available Radiation (PAR). Light availability in aquatic ecosystems is often determined by the diffuse downwelling attenuation coefficient (K_d). Coastal waters are optically complex with three main Optically Important Constituents in addition to water; Colored Dissolved Organic Matter (CDOM), phytoplankton, and Non-Algal Particles (NAPs). Non-algal particles include both inorganic and organic matter, the latter often being detrital in nature. A common benchmark is that water clarity or the K_d(PAR) needs to be sufficient to allow 13 to 22 % of the surface light to reach the eelgrass.

The temporal and spatial variability of water clarity in the Great Bay Estuary was investigated during 2007 with a combination of buoy, boat-based, and Hyperspectral (HS) airborne observations. Buoy observations revealed a strong correlation between the observed PAR attenuation coefficient and the concentration of OICs (r^2 = 0.95). A multivariate model was developed to predict the contribution of each of the OICs to attenuation. Most of the temporal variability in K_d(PAR) at the Great Bay Coastal Buoy location was associated with that due to NAPs. Although the daily mean contribution to attenuation by CDOM and NAPs were of the

same magnitude (around 30%) NAP concentrations varied more than CDOM. Phytoplankton contributed less to the daily mean attenuation, between 12 to 17%.

More detailed analysis of the buoy time-series revealed some of the driving forces of OIC variability. CDOM concentrations were generally inversely related to salinity with higher CDOM levels associated with fresher water indicating the majority terrestrial origin. During times of high flow CDOM concentrations were closely tied to Dissolved Organic Matter (DOC) concentrations in the Lamprey River, the major tributary into Great Bay. The magnitude of this freshwater input of CDOM varied seasonally. As with CDOM, NAP concentrations also increased with increasing levels of freshwater. However, NAP levels were also elevated with wind driven resuspension, a process that lagged wind speed by on the order of one day. The dynamics of phytoplankton variability were more complicated with growth traditionally thought to be either light or nutrient limited. Nitrate levels and phytoplankton abundance at the buoy were inversely related during a bloom at the beginning of the 2007 deployment with nutrients decreasing as the microalgae increased. A subsequent major discharge event reversed this trend.

Hyperspectral aerial remote sensing collections in August and October 2007 were coordinated with extensive in situ validation efforts from multiple teams. In addition to the buoy observations, the in situ measurements included those made continuously along-track, discrete water grab samples, and vertical light profiles. Problems associated with the calibration of the remote sensing system resulted in wavelengths less than 555 nm being unsuitable for inclusion in further analysis. A novel algorithm was developed to predict water clarity with the spectrally limited HS imagery. Retrieved parameters included: total turbidity; absorption, backscattering, and 'effective' attenuation at 555 nm; and the 'effective' K_d(PAR). There was good agreement between the remotely sensed and in situ data which validated the algorithmic approach taken. The in situ and remotely sensed data showed increased concentrations of OICs and associated decreased water clarity in the tributaries. The clearest waters were found in Great Bay (GB), Little Bay (LB), and the Lower Piscataqua Rivers (LPR). Eelgrass survival depths at the 22% surface light level ranged from over 2 meters in these three assessment areas to less than half a meter in others. Survival depths less than one meter indicated an inability to support eelgrass as these water depths would be intertidal (mean water depth less than the tidal range of approximately 2 meters). From these observations it would be predicted that water clarity in Great Bay, Little Bay, and the Lower Piscataqua River was sufficient for eelgrass growth. Absence of eelgrass from any one of these areas is suggestive of factors other than water clarity controlling eelgrass distribution.

Acknowledgements

This work was funded by the Environmental Protection Agency (EPA) as well as the National Oceanic and Atmospheric Administration (NOAA) as part of their Integrated Ocean Observing System (IOOS) program. We would also like to thank Michael Novak who was invaluable with the buoy operations and the in situ survey work. Jeremy LeClair, Colin Edwards, and Chris Nash helped also helped in the collection of field data. Chris Hunt helped processed some of the along-track data. Anna Brook of the Department of Geography and Human Environment of Tel Aviv University provided important aid in the assessment of the quality of the hyperspectral imagery. We are also appreciative for the assistance of the Captain and crew of the R/V Gulf Challenger and David Shay of the Jackson Estuarine Laboratory for their assistance with the deployment and recovery of the buoy.

3 List of Tables

4 List of Figures

5 Introduction

5.1 Estuarine water clarity importance

Increasing nitrogen concentrations (Figure 5.1) and declining eelgrass beds in Great Bay (Figure 5.2) are clear indicators of impending problems for NH's estuaries (NHEP, 2006). The NH Department of Environmental Services (DES) is responsible for developing nutrient criteria for NH's estuaries. DES, in collaboration with the New Hampshire Estuaries Project (NHEP), began this process with the formation of a workgroup in 2005. The NHEP Coastal Scientist, a DES employee, is coordinating the work to undertake this process, with input from the workgroup. Information from the workgroup meetings is available online[1]. This workgroup adopted eelgrass survival as the water quality target for nutrient criteria development for NH's estuaries.

Figure 5.1 Dissolved inorganic nitrogen concentrations in Great Bay (NHEP

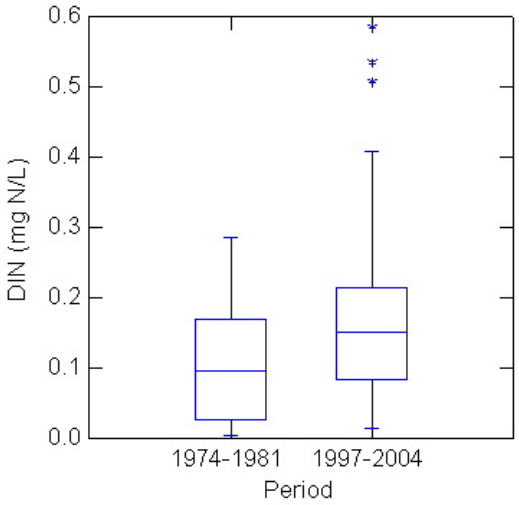

Eelgrass survival is largely dependent on light availability. The NHEP Coastal Scientist has undertaken a review of the water clarity data for NH's estuaries. There are three important constituents in the optically complex coastal waters: phytoplankton, non-algal particulates, and colored dissolved organic matter (CDOM, IOCCG 2000). These constituents, by changing the Inherent Optical Properties (IOPs), affect water clarity or more precisely the magnitude of light attenuation, an Apparent Optical Property (AOP, see Mobley, 1994). Preliminary results indicate that CDOM is the major factor controlling water clarity. However, NHEP is not able to draw strong conclusions from these results because of significant datagaps and a large degree of spatial heterogeneity in NH's estuaries.

Therefore, the NHEP sought funding to support an instrumented buoy in Great Bay, which is managed by the University of New Hampshire (UNH) Coastal Observing Center, to gather sufficient data to resolve uncertainties in relationships between parameters. Funding also supported coordinated collection of spatial data from aerial imagery and continuous along-track surveys to characterize spatial heterogeneity in water quality parameters. The goal of the research was to develop a scientifically defensible conceptual model of the relationships between water clarity and water quality parameters. The conceptual model will be the basis of nutrient criteria for NH's estuaries. A secondary goal of the project was to demonstrate the value of integrating buoy-based measurements with aerial imagery and flow-through surveys to map heterogeneity in water quality parameters within estuarine and near-coastal systems.

[1] www.nhep.unh.edu/programs/nutrient.htm

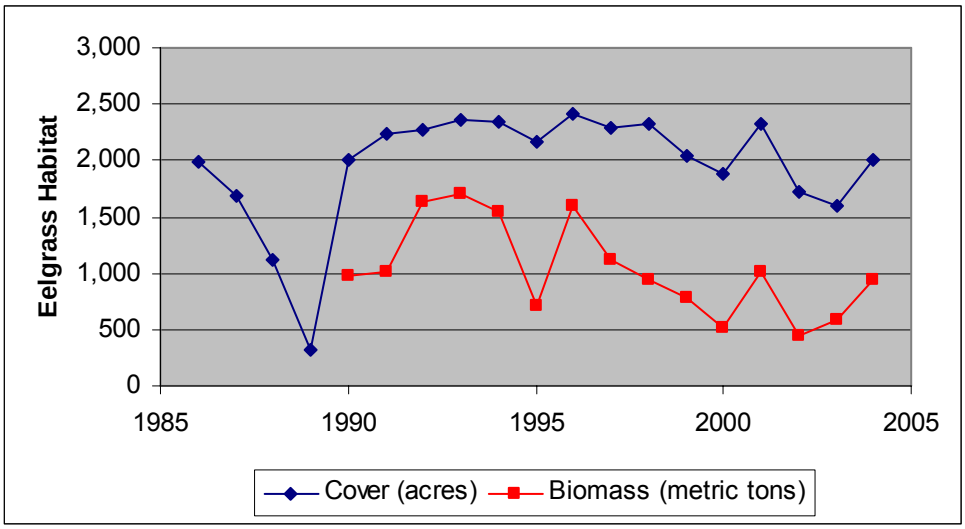

Figure 5.2 Eelgrass cover and biomass in Great Bay (NHEP, 2006)

5.2 Optical Variability – Inherent and Apparent Optical Properties

Coastal and estuarine waters are optically more complex than open ocean waters (Ioccg 2000). Their optical properties depend on four main optically important constituents (OICs); water, plankton (mainly phytoplankton), suspended sediments, and colored dissolved organic matter (CDOM). These constituents together with water affect the magnitude of the Inherent Optical Properties (IOPs) which depend solely on the constituents and the medium. Absorption, scattering, and beam attenuation are common IOPs. In turn, the IOPs together with the angular distribution of the light field affect the magnitude of the Apparent Optical Properties (AOPs). The diffuse downwelling attenuation coefficient and reflectance are common AOPs (see review in Sosik 2007). The downwelling diffuse attenuation coefficient, K_d, is important for calculating light availability to photoautotrophic organisms and can be calculated from two or more downwelling irradiance, E_d, measurements,

$$K_d(\lambda) = -\frac{1}{dz}\ln\left(\frac{E_d(\lambda, z+dz)}{E_d(\lambda, z)}\right), \qquad (5.1)$$

where λ is the wavelength, *z* is the depth, and *dz* is the depth interval. Photosynthetically Available Radiation (PAR) is that available to these organisms capable of driving photosynthesis and commonly refers to visible light which spans 400 to 700 nm. Environmental monitoring programs often measure the PAR attenuation, $K_d(PAR)$.

While IOPs can be calculated as the sum of contributions from OICs this is not strictly the case for AOPs. Nevertheless, this approach has been taken in understanding the effects of biogeographical processes on the optical properties, or bio-optics, of natural waters (Smith and Baker 1978). The simplest model for K_d involves partitioning into contributions from each of the OICs with a concentration and specific attenuation coefficients for each.

$$K_d(\lambda) = K_{d\_w}(\lambda) + [Chl]K^*_{d\_ph}(\lambda) + [CDOM]K^*_{d\_CDOM}(\lambda) + [NAP]K^*_{d\_NAP}(\lambda) \qquad (5.2)$$

Where K_{d_w} is the attenuation for water and the K_d^* terms are the specific attenuation coefficients for phytoplankton, CDOM and NAPs, respectively. As noted by Gallegos (2001), this is the Lambert-Beer law applied to the downwelling diffuse attenuation coefficient, which when applied to PAR is potentially very useful as a management tool.

Based on Monte Carlo model results, Gordon (1989) detailed how the dependency of narrow waveband K_d on the angular distribution of the light field can be minimized for phytoplankton dominated waters (Case I), to make it more closely represent an IOP and more closely follow the Lambert-Beer law. K_d was normalized by the downwelling distribution function, D_0, which accounts for the effects of sun angle, the proportions of direct and diffuse sky irradiance, and the sea state. Application of this approach was also validated in coastal waters where NAPs and CDOM contribute to the optical properties (Case II) so long as large concentrations of non-absorbing particles were absent (Gordon 1989). Again using a modeling approach, Gallegos (2001) expanded on this to further investigate its application to broadband PAR and waters with high suspended solids and found, that while there were some deviations from a strict Lambert-Beer law, strong linear relationships existed between OICs and K_d(PAR).

The turbidity of coastal waters with units of NTU has been used as a measure of optical clarity associated with particles, including both phytoplankton and non-algal particles. As noted by Gallegos (2001), previous studies have noted a near 1:1 relationship between turbidity measured in NTUs and the optical scattering coefficient. Important for this relationship is the backscattering ratio, $b_b\tilde{}$, as the turbidity is essentially a measure of optical backscatter. $b_b\tilde{}$ varies with the type of particle with lower values for phytoplankton compared to non-algal particles (reference). In waters with both phytoplankton and non-algal particles it is important to account of the scattering by phytoplankton if the turbidity is to be used as a measure of the non-algal particles. Total scattering by phytoplankton has been shown to be highly variable as indicated by chlorophyll specific scattering coefficients ranging from 0.06 to 0.60 m^2 mg^{-1} (Morel 1987). Gordon and Morel (1983) determined that,

$$b_p(550) = A[Chl]^{0.62} \qquad (5.3)$$

where b_p is the scattering coefficient and A varied between 0.12 and 0.45 depending on particle type. By examining a large number of transmissometer readings Loisel and Morel (1998) provided a higher estimate of A of 0.78 at 550 nm and a higher exponent of 0.80.

5.3 Hyperspectral Remote Sensing in Shallow waters

Hyperspectral (HS) remote sensing theoretically contains continuous spectral observations and practically has observations every 5 to 10 nm typical of AVIRIS, AISA, PHILLS, and CASI airborne instruments. These sensors typically have tens to hundreds of spectral channels in the ultraviolet (UV), visible, near infrared (NIR), and to the short wave infrared (SWIR) wavelengths. Successfully used for many years with terrestrial applications, this technology has only recently been applied to applications in aquatic systems including those of the coastal oceans (Lee and Carder 2005). Inversion of reflectance signatures in these environments is often complicated as the water column and bottom both contribute to the water leaving radiance with their relative contributions being modulated by water depth (e.g., Lyzenga 1981; Maritorena et al. 1994). A number of approaches have been used for such inversions including; reflectance ratio algorithms (Dierssen et al. 2003), neural networks (Sandage and Holyer 1998), spectral optimization (Lee et al. 2001; Lee et al. 1998; Lee et al. 1999), and spectrum matching and look-up table (LUT, Lesser and Mobley 2007; Louchard et al. 2003; Mobley et al. 2005). Most

of these studies have been performed in relatively clear waters surrounding coral reef environments.

Spectral optimization and the LUT protocols both need information on the range of Inherent Optical Properties (IOPs) of the water column and the bottom reflectance or albedo. However, they differ in how these are used to model and invert remotely measured reflectances. Of the IOPs the absorption and backscattering coefficients (a and b_b, respectively) are of the most importance in remote sensing (Gordon et al. 1988). IOPs are determined in part by water but also by other optically important constituents and can be modeled as proportional to constituent concentrations (Mobley 1994). Optically important in-water constituents include phytoplankton, non-algal particles (both organic and inorganic), and colored dissolved organic matter (CDOM). Bottom reflectance, ρ, depends on the relative contributions of differing substrate types (e.g. sand, seagrass, macrophyte, and coral). The LUT approach uses ranges of constituents, bottom reflectances for differing substrates (and mixtures thereof), and depths with a radiative transfer model such as Hydrolight (Mobley 1994) to predict surface reflectances a priori for a range of conditions. For example, 28 sets of IOPs, 84 depths, and 118 bottom reflectance spectra yielded 275,000 spectra in an LUT (Lesser and Mobley 2007). By matching observed reflectance spectra to the nearest one in the LUT the water column and benthic properties as well as bathymetry are retrieved. In contrast, spectral optimization techniques use a semi-analytical iterative inversion approach to vary water depth, water column optical constituents, and potentially bottom type to minimize differences between observed and predicted spectra. Lee et al. (2001) only used two bottom types sand and seagrass with the bottom reflectance selected before minimization using the remotely sensed reflectance spectra. Goodman and Ustin (2007) used a three-step process to further classify benthic composition. First, a generic bottom reflectance and spectral optimization to invert for water properties and bathymetry; second, these products were used to predict the actual bottom reflectance; and third a linear spectral unmixing model was used for benthic classification. Both LUT and spectral optimization (with unmixing) have demonstrated capacity to retrieve important water column and benthic properties. For example, for each pixel a percent contribution to the bottom reflectance of different substrate and biological cover is possible allowing abundance estimates. However, knowledge of water column optical properties, bottom reflectance and / or bathymetry before the reflectance spectra inversion has the potential to decrease processing time (Mobley et al. 2005) and reduce uncertainties in the retrieved products.

6 Project Goals and Objectives

The project goals were to produce:

a) A single or multi-variate model between the light attenuation coefficient and concentrations of CDOM, turbidity/suspended solids, and chlorophyll-a for the Great Bay system which can be used to develop numeric nutrient criteria;

b) Maps of the distribution of CDOM, turbidity, and chlorophyll-a (and light attenuation using the model described above) on at least two different days for the entire Great Bay system; and

c) A calibrated light availability model for the Great Bay system.

7 Methods

7.1 Buoy

As part of an Integrated Ocean Observing System pilot project the UNH Coastal Observing Center has deployed a Coastal Buoy in Great Bay, NH in ice free months since April 2005 in approximately 7 m of water (43.0715ºN and 70.8678ºW). A bi-moored design ensured the buoy's orientation is maintained. Typically data have been collected from a suite of environmental sensors for 10 minutes either one or two times an hour with a large degree of flexibility in the scheduling possible. The suite of sensors includes ones for physical, chemical, and biological properties as detailed in Appendix 11.1. Data were recorded with an onboard computer (Mooring System Manager, Satlantic Inc.) during activity periods and then telemetered to shore using a dedicated WiFi link at least once an hour. On shore, data were converted to engineering units if appropriate, data outside of the measurement range of the sensors removed, and the mean values for the 10 minute sampling interval calculated. Graphical interpretations and the data are available near real time from the buoy website[2].

Measurements of conductivity, temperature and depth (CTD, SBE37-SIP with tributyl tin antifouling plugs, Seabird Inc.), nitrate (ISUS, Satlantic Inc.), turbidity and chlorophyll-a (ECO-FLNTUS, WET Labs Inc.), and CDOM (ECO-FLCDS, WET Labs Inc.) immediately beneath the buoy at a depth of ~ 0.93 meters. For biofouling mitigation both ECO sensors were equipped with copper face-plates and copper shutters with wipers. The turbidity sensor for the second deployment in 2007 was also calibrated to provide particulate optical backscattering coefficient at 700 nm, $b_{bp}(700)$. Nitrate concentrations were determined just prior to the duty cycle used for the rest of the instruments due to the power requirements of the ISUS. The sensors are calibrated in the laboratory, either at UNH or by the manufacturers, at least annually and field calibration and validation samples are collected during regular buoy visits. Cleaning of certain sensors during these field trips has proven essential to maintaining data quality. Typically the buoy has been deployed in April, recovered and turned around in July or August, and recovered in early December before the onset of ice.

In 2007 hyperspectral irradiance measurements were obtained at the surface, $E_s(\lambda)$, and at 1 m, $E_d(\lambda,1m)$, with a spectral resolution of ~3.3 nm between 350 and 800 nm (HyperOCR, Satlantic Inc). Upwelling radiance was also measured underwater but was not used in this study. Copper Bioshutters (Satlantic Inc.) minimized biofouling on the underwater radiometer but regular cleaning of the sensors was necessary. To minimize the effect of the buoy's structure on the measured underwater irradiance the subsurface radiometer was mounted on an arm to the south of the buoy. This kept the radiometer approximately 1 m away from the nearest part of the buoy's structure and in situ estimates of the sensor depth by divers had a mean of 1.00 m (range 0.94-1.10 m).. Every 10 light measurements an internal shutter in the radiometers blocked the light path enabling dark measurements to be acquired. After interpolation for time these dark readings were subtracted from the light measurements. Interpolation to a common wavelength framework (every 5 nm between 350 and 800 nm) allowed for comparison of results from radiometers with differing individual wavelengths. Radiometers were calibrated annually at the manufacturers with a NIST traceable light source. After converting to quantum units the downwelling PAR irradiance was calculated by integrating between 400 and 700 nm.

[2] http://www.cooa.unh.edu/buoydata/buoy.jsp

7.1.1 Other sampling at the buoy during the year

During weekly sampling trips, vertical profiles of physical and optical properties were collected as well as discrete water samples adjacent to the buoy. Comparison of these measurements with readings returned by the buoy sensors allowed calibration and validation. A custom profiler measured conductivity, temperature, and depth (Fastcat 49 CTD, Seabird Inc.), chlorophyll-a and CDOM (ECO-triplet fluorometer, WET Labs Inc.), and particulate backscatter (bb-9, WET Labs Inc.). Similar to the buoy these sensors were calibrated annually by the manufacturer but were not subject to fouling. Hyperspectral measurements of the absorption and attenuation of both whole and filtered water (ac-s, WET Labs Inc.) were also measured with the profiler. As part of a river monitoring campaign dissolved organic carbon was measured on Lamprey River water samples filtered through pre-combusted Whatman GF/F glass fiber filters using high-temperature platinum-catalyzed combustion (Shimadzu TOC-V; non-purgeable organic carbon mode). The DOC samples were collected adjacent to the Packers Falls USGS stream gage station (#01073500) from which daily stream flow is available since 1934.

7.1.2 Buoy Irradiance analysis

Analysis of the irradiance data presented two challenges; 1) transmitting the surface irradiance through the air-water interface so that K_d could be calculated, and 2) correction for the variations in the geometrical distribution of the light field. Both of these can be dealt with varying levels of complexity.

For transmittance the simplest surface correction involves a single factor 0.965, so 96.5% of the light passes through the interface. This has been shown to be valid for optimal conditions with solar zenith angles less that 45º as well as clear skies and low wind (e.g., Morel and Antoine 1994; Morel and Maritorena 2001). More complex corrections require the surface irradiance to be split into direct and diffuse components and knowledge of the surface roughness (e.g., Sathyendranath and Platt 1988). Direct sunlight transmittance can be calculated using the Fresnel equation while that of diffuse light can be approximated to 94.5% (Sathyendranath and Platt 1988). Surface roughness, often modeled from wind speed, is most important with high solar zenith angles (>50º) and can increase transmittance (Mobley 1994; Preisendorfer and Mobley 1985; Preisendorfer and Mobley 1986).

Light field distribution corrections, such as that of Gordon (1989), try to minimize the effects of the light field (including incident distribution and surface effects) so that K_d more closely resembles an IOP (Mobley 1994). The simplest correction is for direct sunlight when multiplication of K_d by the cosine of the refracted solar zenith angle below the surface. Gordon (1989) took this further and includes the proportion of direct to diffuse irradiance as well as effects of surface roughness (wind driven gravity waves).

Due to the constraints of buoy measurements, the relative contributions of the direct and diffuse irradiance were estimated using a modeling rather than the observational approach suggested by Gordon (1989). For each measurement time clear sky direct and total surface irradiances, E_{s_direct} and E_{s_total}, were estimated every five nanometers between 350 and 800 nm using the SBDART atmospheric radiative transfer model (Ricchiazzi et al. 1998). The model was initialized with the time and location obtained from the buoy GPS, the model supplied seawater surface albedo, wind speed measured on the buoy, and defaults for the rest of the parameters. PAR irradiances were calculated by integrating the obtained spectra as described above.

For both the individual wavelength and the PAR modeled surface irradiances, the direct sun fraction of the subsurface irradiance, f, was calculated after Gordon (1989). For this it is

necessary to have the surface transmittance for both direct and sky irradiance; the Fresnel equations (e.g., Mobley 1994) provided transmittance for the direct fraction from the solar zenith angle and transmittance for the diffuse sky fraction was set at 0.9382, the median transmittance for θ between 0 and 80°. The effect of surface roughness caused by wind stress on transmittance was ignored in this study partly because no simple parameterization was available. The sky state was determined by comparing the measured and modeled total surface PAR irradiance. Similar to Huot et al. (2007), where the ratio of measured to modeled surface irradiance was greater than 80% both direct and sky irradiances were assumed to exist and the calculated f value chosen. For ratios less than 80% the direct contribution was assumed to be negligible and f set to 0. The downwelling distribution function, D_o, was calculated again with a relationship of Gordon (1989) using f and θ_{sw}. The surface irradiance measured above the water was then transmitted across the air-water interface using the sky state adjusted f.

7.1.3 Buoy calibration, validation, and data processing

Initial processing of the ECO-FLNTUS data for the second deployment during 2007 indicated a high degree of variability in both chlorophyll-a and turbidity measurements. This was characterized by sudden spikes in values that were not present in other data. Two distinct sets of measurements were observed in the10 minute sampling records, one set close to or at the saturation values of the sensors and the other much lower. Increased signal due to detection of fouling macroalgae on the buoy or sloughed eelgrass passing by were the probable cause for the spikes. Sample records were determined to be compromised if the coefficient of variation was greater or equal to 10%. For these records the mode of data not in the saturating set were used as the representative values.

Constituent concentrations determined from the discrete water samples were significantly related to those from the buoy (Table 7.1). Generally there was 1:1 agreement between the two datasets apart from the chlorophyll-a concentration. The chlorophyll analysis suggested that the factory calibration of the buoy sensor underestimated the chlorophyll concentrations in these waters. Consequently, only the chlorophyll-a data from the buoy data was adjusted using the validation data set. The linear regression results (Table 7.1) indicated that at zero chlorophyll the buoy would still read 1.12 $mg.m^{-3}$. However this was greater than the minimum value observed by the buoy of 0.70 $mg.m^{-3}$ and that correction with parameters from Table 7.1 would have resulted in negative concentrations. The buoy chlorophyll correction coefficient was calculated by subtracting the minimum observed value at the buoy and forcing a regression through the origin, which indicated that the buoy after the subtraction readings were too low by a factor of 2.70.

Table 7.1 Buoy validation results

SENSOR (Manufacturer)	PRESENTED PARAMETERS	SLOPE	INTERCEPT	DISCRETE VALIDATION (r^2)
SBE37-SIP (Seabird)	Temperature	1.044	-0.438	0.99
	Salinity	0.989	-0.245	0.99
FLCDS (WetLABS)	CDOM	0.996	-2.833	0.98
FLNTUS (WetLABS)	Chlorophyll-a	0.306	1.115	0.77
	Turbidity (715 nm)			0.96
OPTODE (Aanderaa)	Dissolved oxygen	1.068	-22.868	0.87
ISUS (Satlantic)	Nitrate	1.435	-3.881	0.86

For the analysis of the attenuation coefficients data were restricted to times when the solar zenith angle was less than 70°, PAR measurements at both surface and 1m were greater than zero, whole turbidity measurements were less that 48 NTUs (sensor saturated at ~48 NTUs), and adjusted buoy chlorophyll measurements were less than 25 mg m^{-3} (above this were data not considered corrected by the mode method detailed above). Data were also screened for bio-fouling of the E_d sensor which was the most prone to this problem. For this a combination of known fouling events from direct diver observations and data quality control was used.

7.2 Spatial sampling on day of hyperspectral imagery

7.2.1 Continuous along-track sampling

Coincident with the hyperspectral imagery collections in August and October, two continuous along-track surveys were conducted throughout the study area from a small boat. Some of the grab samples as well as vertical profiles at some stations were also collected using this vessel. Water from just below the surface was pumped through a custom instrumentation package measuring conductivity and temperature (Seabird SBE45), CDOM and chlorophyll-a (separate WETStar fluorometers, WET Labs Inc.), beam attenuation (C-Star transmissometer, WET Labs Inc.), light absorption and attenuation at nine wavelengths (ac-9, WET Labs Inc.), optical backscattering at three wavelengths (ECO bb3, WET Labs Inc.), and dissolved oxygen (Optode, Aanderaa Instruments Inc.). Measurements are spatially and temporally referenced by simultaneous GPS and time data acquisition by a single computer. Datastreams are recorded at variable rates but most are around 1 Hz.

The diffuse attenuation coefficient (K_d) and the remote sensing reflectance (R_{rs}, both apparent optical properties) were estimated from along-track absorption and scattering coefficients (a and and b, respectively). The downwelling diffuse attenuation coefficient was estimated with the relationship of Gordon (1989) such that,

$$\frac{K_d(\lambda)}{D_o} = 1.0395(a + b_b) \qquad (7.1)$$

where D_o is the downwelling distribution function, a the absorption coefficient, and b_b the backscattering coefficient. This is relationship functionally similar to that of (Lee et al. 1998; Lee et al. 1999) for the "effective" attenuation coefficient (see Box 7.1). K_d(PAR) can then be estimated by integrating the spectral $K_d(\lambda)$ weighted for the irradiance spectra between 400 and 700 nm. The spectral weighting function for incident radiation is approximately uniform for units of µmol photons m^{-2} s^{-1}. One estimate of the remote sensing reflectance calculated with the parameterization of Gordon et al. (1988).

$$r_{rs} = \sum_{i=1}^{2} l_i (b_b / (a + b_b)^i, \qquad (7.2)$$

$$l_1 = 0.0949, l_2 = 0.0794$$

7.2.2 Grab samples

During the two days of aerial data collection, grab samples for water quality assessments were collected at stations throughout the study area. Three separate teams were in the field during the overflights for sample collection. Sixteen stations were occupied on Aug. 29 and 15 were sampled on Oct. 17. It was not possible to visit all 21 proposed stations due to a low tide

sampling period on both days. Water samples were collected in acid-washed LDPE or HDPE bottles and transported back to Jackson Estuarine Laboratory for processing. Field replicates were collected and analyzed for each parameter. Two triplicates were collected Aug. 29 at GRBAP and NH04-245C. On Oct. 17, one triplicate was taken at NH04-245C.

Samples for chlorophyll-a analysis were processed, stored and analyzed according to accepted protocols for satellite ocean color sensor validation (Mueller et al. 2003). The protocol for TSS followed the procedure given by Strickland and Parsons (1972) in accordance with accepted protocols for satellite ocean color sensor validation (Mueller et al. 2003). Samples for CDOM and absorption spectra analysis were processed, stored and analyzed according to accepted protocols for satellite ocean color sensor validation (Pegau et al. 2003). Phosphate concentrations were determined following EPA Method 365.2. Chlorophyll-a, TSS, CDOM, absorption spectra and phosphate measurements were made in the Coastal Observing Laboratory in Durham, NH. Nitrate + nitrite determinations were performed by the Water Quality Analysis Laboratory in Durham, NH following EPA Method 353.3.

7.2.3 Direct *In Situ* Measurements

In addition to the collection of water samples at every accessible station, each of the three teams was equipped with different types of instrumentation. The DES Shellfish Program group used a YSI 30 to obtain temperature and salinity data at the following stations on both Aug. 29 and Oct. 17: NH-0057A, NH-0058A, NH-0062A and GRBSF.

Scientists representing the UNH Great Bay NERR System Wide Monitoring Program and the UNH National Coastal Assessment Program visited the following sites on both Aug. 29 and Oct. 17: GRBGB, GRBSQ, GRBLR, GRBCL, GRBAP, GRBOR, NH-0049A and NH-0052A. They used a YSI 85 to collect temperature and salinity data as well as a Licor 1400 for measurement of photosynthetically active radiation (PAR) in the water column.

The UNH Coastal Observing group visited GB4A, GRBAP, GRBGB, NH04-235C and NH04-245C on both Aug. 29 and Oct. 17. On Aug. 29, NH00-0027B was also sampled. A custom profiler measured conductivity, temperature, and depth (Fastcat 49 CTD, Seabird), chlorophyll-a and CDOM (ECO-triplet fluorometers, WET Labs Inc.), absorption and attenuation (ACS meter, WET Labs Inc.) and particulate backscatter (bb-9, WET Labs Inc.). A Satlantic Hyperpro II was used to determine AOPs at each of these stations.

7.3 Hyperspectral imagery

The hyperspectral imagery collected information for the Great Bay estuarine system of NH and Maine. This area encompassed the Great Bay, Little Bay, Piscataqua River and some or all of the tidal portions of the Winnicut, Squamscott, Lamprey, Oyster, Bellamy, Cocheco and Salmon Falls Rivers. Approximately 40 square kilometers of estuarine waters were part of the study area. The initial plans were to collect imagery during two differing flow regimes for the estuarine system during low-flow summer and higher-flow fall conditions. The goal was also to collect data at either high or low tide when temporal consistency would be maximal.

The overflights were conducted by SpecTIR (www.SpecTIR.com). SpecTIR proposed an airborne data collection with the VNIR sensor with a spatial resolution of 2.5 meters for the area of interest, and a nominal spectral resolution of 10nm or 64 spectral channels from approximately 430 nm to 1000 nm (Table 7.1). Navigation was performed with high speed airborne DGPS integrated with a laser ring gyro and deliverables were calibrated radiance and geographic lookup tables with navigation. SpecTIR also recommended that overflights should

coincide with solar zenith angles less than 60º to minimize sunglint contamination and have minimal cloud cover.

Table 7.2 Acquisition parameters for the hyperspectral data collection

Sensor System:	ProSpecTIR-V
Spectral Range:	400-1000nm
Spectral Resolution:	10nm
Number of Bands:	64
Ground Spatial Distance (GSD):	2.5m

7.3.1 Radiance processing

Radiometric calibration by SpecTIR was achieved through the use of a Labsphere USS-2000-V uniform source. This 20-inch diameter integrating sphere was equipped with three internal 45 watt and one 75 watt externally mounted halogen light sources. Each lamp was powered by separate DC regulated constant current power supplies and the addition of a variable attenuator provided even more precise control of light levels. Luminance output was variable from 0 to 4000 foot-lamberts and measured uniformity was > 98% over the entire 8-inch exit port. This sphere carried a NIST traceable spectral radiance calibration from 400nm to 2500nm at a sampling interval of 10nm. The resultant calibration allowed SpecTIR to provide data that was theoretically within +/- 5% of absolute radiance. However, problems were associated with the calibration at blue wavelengths (see Appendix 10.1).

Wavelength calibration was generated and monitored through a characterized Mercury-Argon (HgAr) emission lamp source. HgAr lamps are a common spectral calibration source for spectrometers and provide several fine distinct emission lines in both the VNIR and SWIR spectral domain allowing for accurate wavelength mapping. During processing, flight data QA/QC procedures relied on well documented atmospheric features such as the Oxygen fraunhaufer line at 760nm to ensure that accurate wavelength mapping was maintained.

Dark current measurements were included at the end of each flight line. The first step of processing was to remove the dark current "signal" from the imagery. The calibration gain file was then applied to convert the raw data values to radiance units.

7.3.2 Atmospheric correction

The radiances provided by SpecTIR were those collected at the sensor which included both surface and atmospheric components. The TAFKAA atmospheric correction package was incorporated into the ENVI processing software and used to remove the atmospheric component and calculate the surface remote sensing reflectance (Gao et al. 2000; Montes et al. 2001). A spatially consistent atmosphere for the times of data collection was assumed as the wavelength range did not include SWIR channels necessary for the aerosol determination mode in turbid waters.

For the August 29th data collection the ozone content was set to 289 atm-cm (289 DU, data from NASA Ozone processing team, TOMS). Water vapor content (2.3 cm) and aerosol properties (aerosol optical depth of 0.17) were obtained from the Aeronet-processed Thompson farm Cimel Sun photometer operated by the UNH AIRMAP group. Other atmospheric gasses were left as default including NO_2 which has a column value of 5 x 10^{15} molecules.

Results from the atmospheric correction and other evaluation procedures for the hyperspectral aerial information indicated that there were problems with data in the blue wavelengths. This was ultimately confirmed by the contractor so only information with wavelengths of 555 nm or above were suitable for the further analysis (further details of the atmospheric correction and quality evaluation procedures are available in Appendix 10.1).

7.3.3 Area isolation

The hyperspectral imagery contained information not only on the waters of the Great Bay Estuary but also of the surrounding watershed. The first task in processing the HS imagery was therefore masking out the land pixels. This procedure is required in order to avoid similar features in the surrounding watershed (such as other water bodies or similar sand) to be classified in the next processing steps. The unsupervised classification was applied to on each line (20-25 classes with a change threshold of 3.5%). The resulting output is a hyperspectral image that contains null values in all areas surrounding Great Bay Estuary (example in Figure 7.1)

A

B

Figure 7.1 Hyperspectral imagery (line 0829-0545) before (A) and after (B) masking out the land pixels of the surrounding watershed areas,

Pixels with Submerged Aquatic Vegetation (SAV) were determined with the algorithm of Lee (2001) such that $R_{rs}(555) > 0.01\ sr^{-1}$ and $R_{rs}(710)/R_{rs}(670) < 1.2$. The 1.23 cutoff for the ratio

was determined by visual inspection of the hyperspectral imagery. Deep water pixels with low turbidity were isolated with a threshold based on the above reflectance ratio for SAV detection and $R_{rs}(584)/R_{rs}(688) < 1$. Initial estimates of deep areas using this approach were augmented with additional manual area selection due to problems associated with the similarity of the spectral signatures of some shallow sandy and highly turbid deep areas.

7.3.4 Water quality

The relationship between the remote sensing reflectance and the IOPs of Lee et al. (Lee and Carder 2005; Lee et al. 2001; Lee et al. 1998; Lee et al. 1999) were utilized as the theoretical background for the inversion of the HS imagery (Box 7.1). Further, the Quasi Analytical Algorithm (QAA) approach to obtain IOPs of Lee et al. (2002) was adapted for the current HS imagery as detailed below.

Box 7.1 Lee et al. algorithm for hyperspectral remote sensing in shallow waters

$$R_{rs} \approx \frac{0.5 r_{rs}}{1 - 1.5 r_{rs}} \tag{7.2}$$

$$r_{rs} = r_{rs}^{dp}\left[1 - \exp(-D_0 + D_1(1 + D_1^{'}u)^{0.5})\kappa H\right] + \frac{\rho}{\pi}\exp(-D_0 + D_2(1 + D_2^{'}u)^{0.5})\kappa H) \tag{7.3}$$

$$r_{rs}^{dp} \approx (0.084 + 0.170u)u \tag{7.4}$$

$$\kappa = a + b_b \tag{7.5}$$

$$u = b_b/(a + b_b) \tag{7.6}$$

$$b_{bp}(\lambda) = b_{bp}(\lambda_0)\left(\frac{\lambda_0}{\lambda}\right)^{\eta} \tag{7.7}$$

Equation 7.7 after

Symbol	Description	Units
R_{rs}	above water remote sensing reflectance	sr^{-1}
r_{rs}	below water remote sensing reflectance	sr^{-1}
r_{rs}^{dp}	r_{rs} for optically deep waters	sr^{-1}
D coefficients	parameterization specific coefficients	
κ	"effective" diffuse attenuation coefficient	m^{-1}
H	bottom depth	
ρ	bottom reflectance	
b_b	backscattering coefficient	m^{-1}
a	absorption coefficient	m^{-1}
η	scattering exponent	

Turbidity in optically deep waters – was estimated using the remote sensing reflectance at 708 nm. After conversion to remote sensing reflectance just under the water-air interface (Equation 7.2) b_b was calculated assuming that the absorption by optically important constituents apart from water was negligible ($a_w(708) = 0.785\ m^{-1}$ and Equations 7.4 and 7.6). Turbidity was calculated by converting backscattering to total scattering with the backscattering coefficient (~0.0215) and the observation that total scattering and the turbidity in NTU scale with a 1:1 relationship (Gallegos 2001).

Absorption in optically deep waters – was calculated by extrapolating the estimate of the particulate backscattering coefficient at 708 nm to 555 nm (Equation 7.7) after removing water

backscatter. The exponent η (0.755) was determined from IOP profiler measurements. Total absorption at 555 nm was then determined from total backscatter and the remotely sensed information (Equations 7.4 and 7.6).

Downwelling Attenuation coefficient – Gordon et al. (1989) provided a similar expression for the downwelling attenuation coefficient (normalized by the downwelling distribution function, D_0) to Equation 7.5 which was used to calculate $K_d(555)$. Gallegos (2001) noted that $K_d(555)$ was closely related to $K_d(PAR)$ and observations at the buoy confirmed this. Greater than 99.3% of the variability in $K_d(PAR)$ was explained by $K_d(555)$ such that,

$$K_d(PAR) = 0.930 \times K_d(555) + 0.290 \quad (7.8)$$

7.4 Converting between units

Multiple units are used to parameterize similar quantities that can lead to confusion when comparing results from different analytical techniques. For example, the particle load of a water body can be expressed as turbidity with units of NTU, particle backscatter with units of m^{-1}, and as the gravimetric concentration with units of g L^{-1}. Ideally these measurements should scale linearly although practically this is often not the case due to differences in the responses of particle types (e.g. mineral versus organic). Similarly, CDOM concentrations are traditionally given in terms of absorption at a set wavelength with units of m^{-1} but the fluorometers used in both the continuous along-track and buoy systems are calibrated in ppb quinine sulphate equivalents (ppb QSE). Using observations made as part of this study and others within the geographic vicinity of the coastal Gulf of Maine relationships were established for conversion between units (Table 7.3). It should be noted that these relationships are approximate and that spatial and temporal changes in the qualitative nature of the observed constituents can lead to changes in the conversion factors.

Table 7.3 Conversion factors

Conversion	Value	Units	Derivation
Turbidity to optical particle backscatter at 715 nm, $b_{bp}(715)$	0.0144	$m^{-1}NTU^{-1}$	Buoy FLNTUS and IOP profiler bbp
	0.0215	$m^{-1}NTU^{-1}$	Backscattering ratio on August 29, 2007
Total Suspended Matter (TSM) to turbidity	0.51	NTU $g^{-1}L$	Median ratio from SWMP
	0.30	$NTUg^{-1}L$	Gallegos (2001)
$a_{CDOM}(440)$ to ppb QSE	27.00	QSE ppb m	Buoy FLCDS, IOP FLCDS and grab samples

8 Results and Discussion

8.1 Buoy

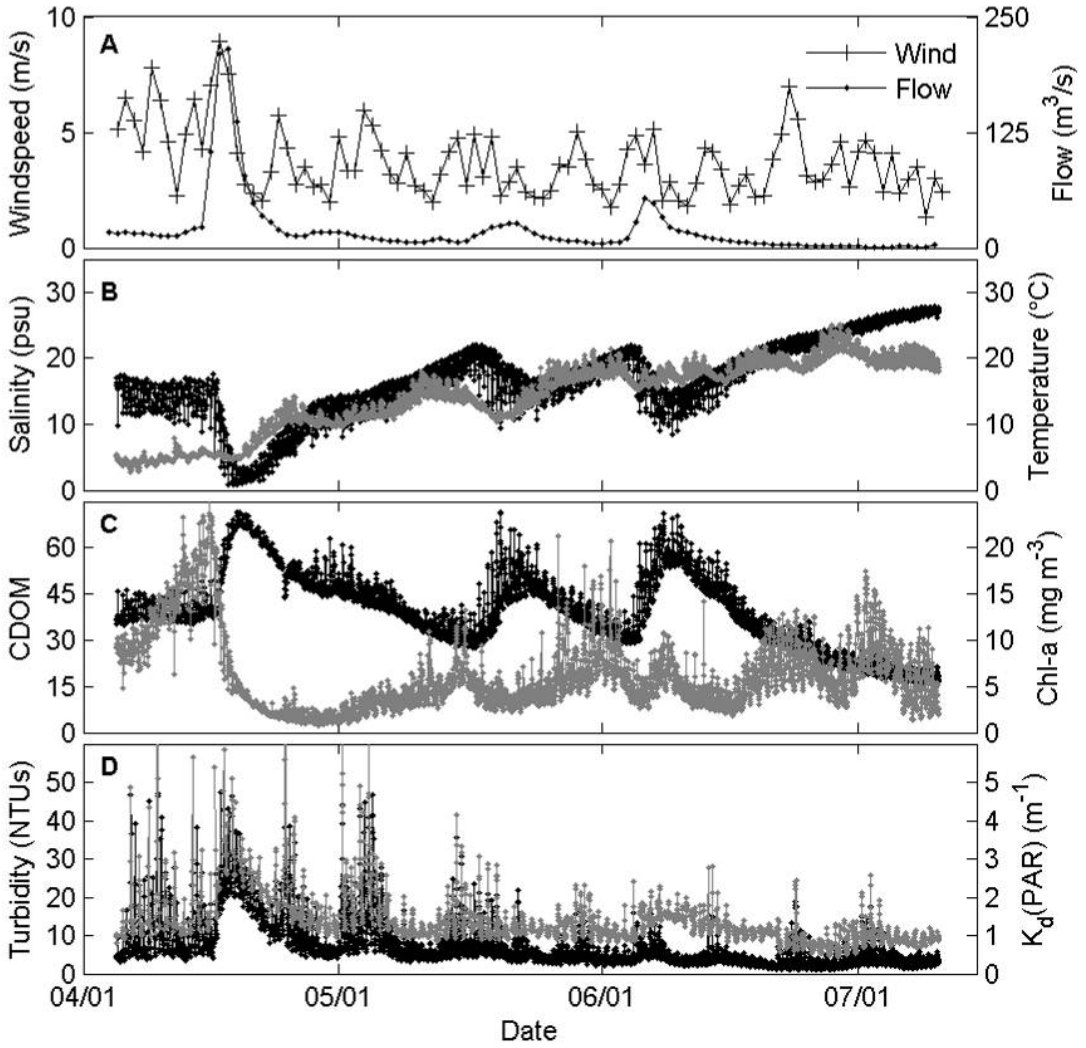

Figure 8.1 Time-series of measurements at the Packers Falls USGS stream gage station (#01073500) in the Lamprey River and at the Great Bay Coastal Buoy between 4 April and 10 July, 2007. For the bottom three panels the y-axis on the left is associated with the black line and the y-axis on the right the grey. A) Daily average windspeed (measured at the buoy) and river flow clearly indicating the high winds and flows associated with storms especially the largest in mid April. B) Salinity and temperature both increased with the transition to summer months. The large storm and associated rainfall in the middle of April decreased the salinity to less than 1 psu. C) The increased discharge was associated with elevated Colored Dissolved Organic Matter (CDOM) and appears to have halted a phytoplankton bloom as indicated by decreasing chlorophyll-a concentrations (Chl-a). D) The turbidity and the PAR downwelling diffuse attenuation coefficient, K_d(PAR), not only increased during the April storm but also with high wind events.

Between 04-Apr-2007 20:00 and 6-Dec-2007 17:10 GMT there were 10784 activity periods on the buoy. During that time there were 5540 light measurements of which 3207 passed the initial standards detailed above. Most variables measured showed a wide range of values with the

influence of tidal, diurnal, and episodic event driven processes apparent (Figure 8.1). The effect of the large river discharge associated with the storm on April 16 was clearly observed in the salinity which reached a minimum on 18-Apr-2007 01:00 GMT of 0.78 psu (Figure 8.1B). This increased runoff in April resulted in increased CDOM and nitrate levels and appeared to have halted a phytoplankton bloom that had been building since the beginning of the deployment with the phytoplankton being flushed from Great Bay at this time (Figure 8.1C). The attenuation coefficient and the turbidity closely tracked each other with maxima appearing to occur after high wind events (Figure 8.1D).

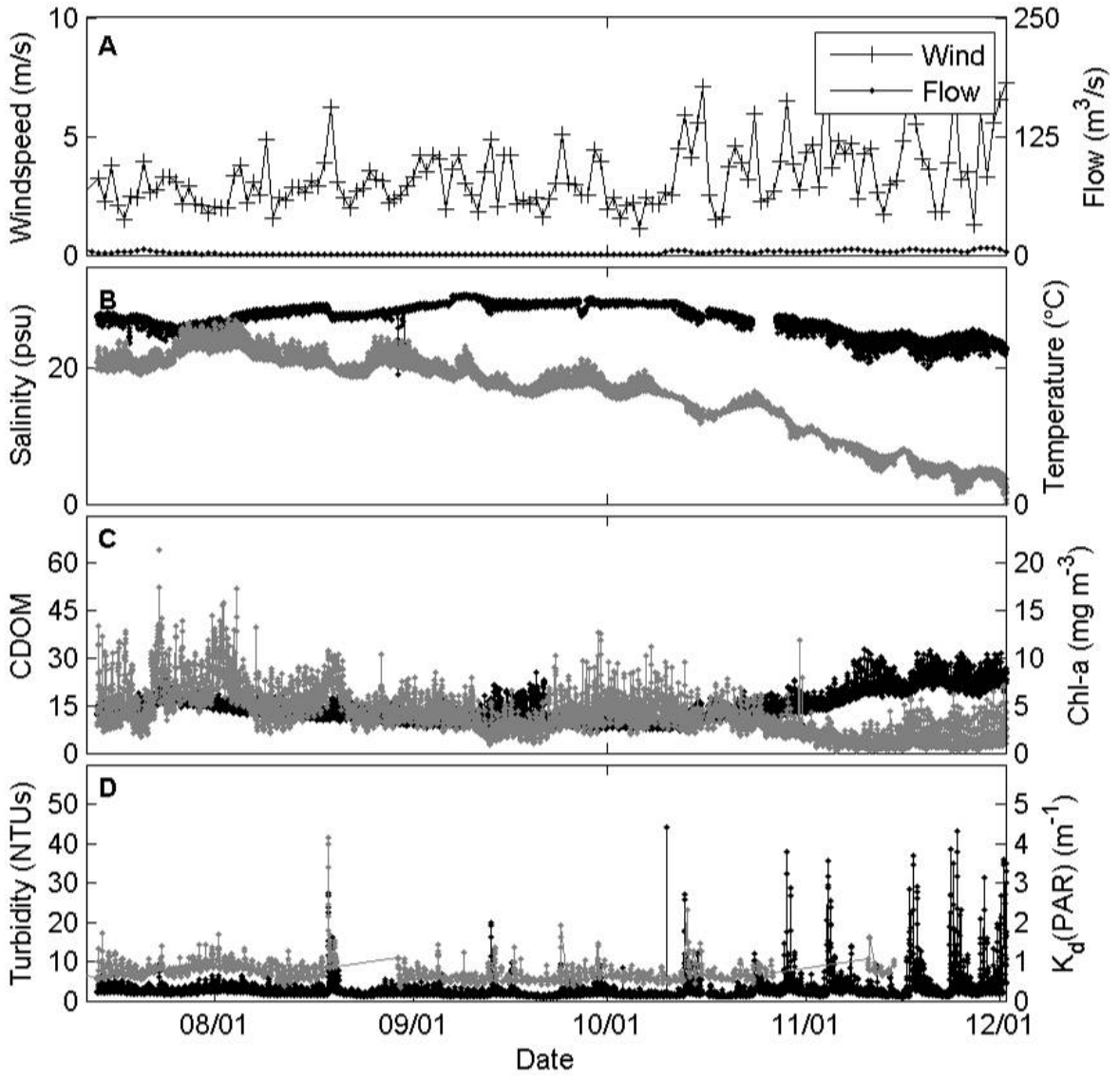

Figure 8.2 Time-series of measurements at the Packer's Falls USGS stream gage station (#01073500) in the Lamprey River and at the Great Bay Coastal Buoy between 13 July and 1 December, 2007. As with Figure 8.1, for the bottom three panels the y-axis on the left is associated with the black line and the y-axis on the right the grey. Panels and scales are the same for Figure 8.1.

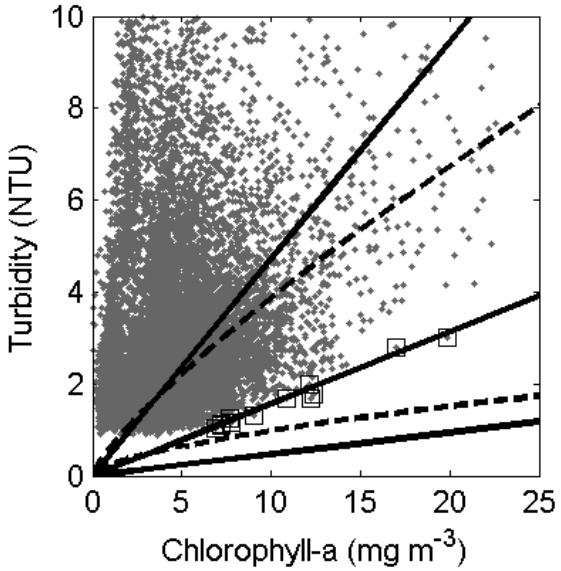

Figure 8.3 In general turbidity was not related to chlorophyll-a concentration. However for a group of points (squares) there was a significant linear relationship between turbidity and chlorophyll-a. This relationship was within the range of historical chlorophyll scattering models including linear estimates of $b^*(550)$ of 0.06 and 0.60 m^2 mg^{-1}, bottom and top solid lines, respectively, and the power functions of Gordon and Morel (1983) and Loisel and Morel (1998), bottom and top dashed lines, respectively. Previous scattering models were adjusted to NTUs measured at 700 nm with correction factor $^{550}/_{700}$ to adjust for wavelength,.

There was no clear dependency of the turbidity on the chlorophyll-a concentration (Figure 8.3). The lower boundary of the relationship did appear to indicate that increasing chlorophyll resulted in increasing turbidity. A group of 13 points with the least turbidity per unit chlorophyll was linearly related to the chlorophyll-a concentration ($F = 424$, $p<0.01$, $r^2 = 0.975$), with a slope of 0.157 NTU. m^3 mg^{-1} with an intercept that was not significantly different from zero (-0.05 NTU, $t = 0.5$, $p<0.01$). We used the previously noted near 1:1 relationship between the scattering coefficient and turbidity measured in NTU (Gallegos 2001) to assess this relationship in light of historical models for phytoplankton scattering . The observed relationship was encompassed by these previous scattering models (Figure 8.3, Gordon and Morel 1983; Loisel and Morel 1998). The turbidity from non-algal particles was estimated by subtracting current model predicted phytoplankton turbidity from the total.

A multiple linear regression was used to assess the contribution of each of the three optically important constituents to $K_d(PAR)$ adjusted with D_o, using Equation 5.2. The regression showed a significant relationship between the attenuation coefficient and the constituents ($F= 20650$, $p<0.01$, Figure 8.4) with the constituents explaining 95.09 % of the variability in $K_d(PAR)/Do$. The multivariate model is given by

$$\frac{K_d(PAR)}{D_o} = 0.2449 + 0.0188.[Chl] + 0.0101.[CDOM] + 0.0784.[NAP] \qquad (8.1)$$

with the units of the concentration terms reflecting those used by buoy instrumentations, ([Chl] in mg m^{-3}, [CDOM] in ppb QSE, and [NAP] in the chlorophyll adjusted turbidity (NTU) as described above.

Table 8.1 Coefficients for the optically important constituents coefficient given in Equation 3 derived by multiple linear regression.

Optically Important Constituent	*Coefficient*	*Standard Error*	*t Stat*	*P-value*
K_d-w	0.2449	0.0050	48.2	<0.001
CDOM	0.0100	0.0002	63.2	<0.001
CHl-a	0.0188	0.0007	27.2	<0.001
NAP	0.0784	0.0005	153.2	<0.001

All coefficients were significantly different from zero (Table 8.1) and, where the same units were used, were similar to values reported historically such as those derived from modeling by Gallgegos (2001). The median RMS error was 0.0594 m^{-1} or approximately 7.7%. Gallegos reported mean specific coefficients for chlorophyll of 0.0154 m^2 (mg chl-a)$^{-1}$ and

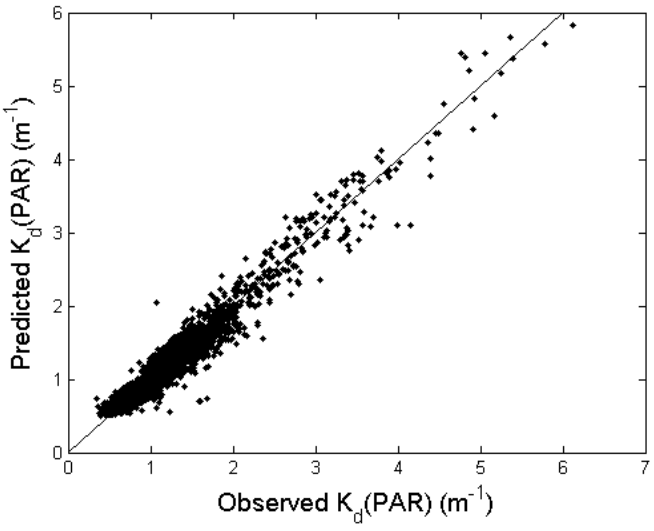

Figure 8.4 The observed K_d(PAR) and that predicted using the Equation 3. The median RMS error was 0.0594 m^{-1} or 7.7%

It should be noted that, despite the high degree of correlation between the K_d(PAR) values and the concentrations of chlorophyll-a, CDOM, and NAPs recorded at the buoy, apparent optical properties such as K_d are not strictly linearly additive. The normalization of K_d with the downwelling distribution function, D_o, does not completely alleviate some of the associated uncertainties but not completely. The linear-additive relationship is further complicated by: using a broad spectral band such as PAR, temporal and spatial variability in the underlying IOPs of the optically important constituents including non-linear effects, and other factors not taken into account. However, despite these potential sources of uncertainty, the high correlation suggests that this multivariate approach is applicable for the waters surrounding the Great Bay Coastal Buoy.

Contributions to K_d(PAR) by Optically Important Constituents

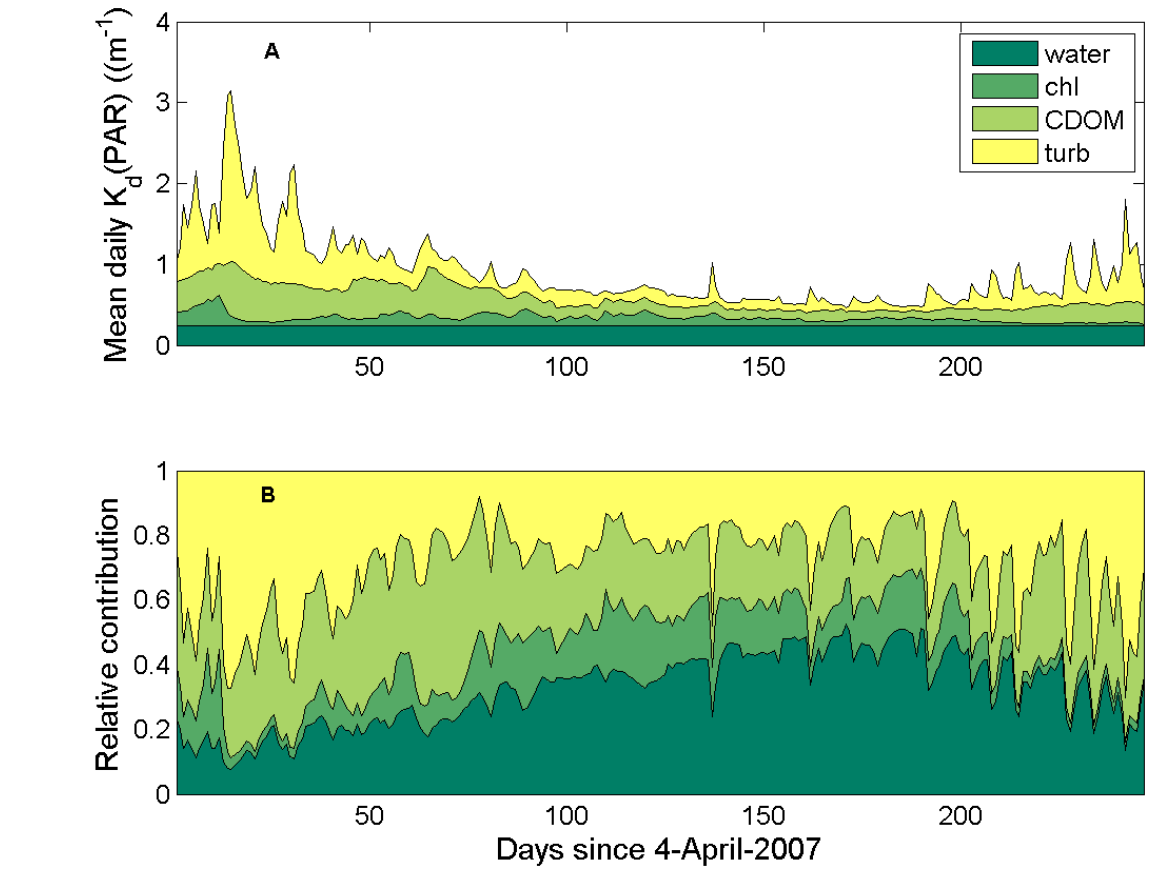

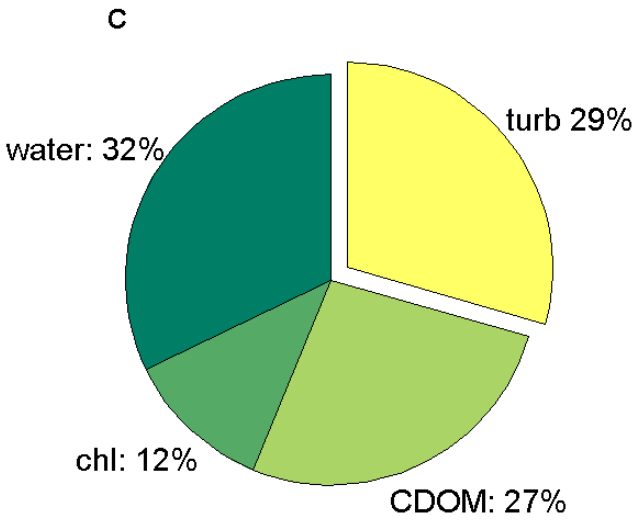

Figure 8.5 Contributions of the optically important constituents to K_d(PAR) measured at the Great Bay Coastal Buoy. A) The daily averaged K_d(PAR). B) The relative contribution. C) The mean daily contribution of each component. The water contribution reflects that derived by the multiuple linear regression of 0.245 m^{-1} which is higher than that estimate by Morel et al. (2007) of 0.1544 m^{-1}.

8.1.1 CDOM variability and Lamprey river DOC

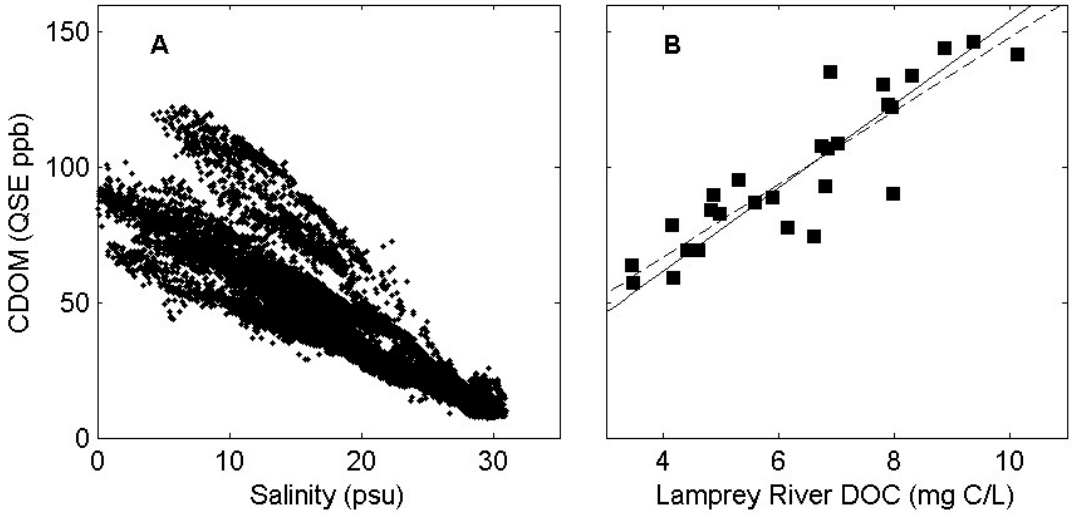

Figure 8.6 A) Overall CDOM concentrations measured at the buoy were negatively correlated with the salinity over a wide rage of salinities encountered during the ice-free months of 2005, 2006 and 2007. This was indicative of mixing between high CDOM concentration freshwater inputs and low CDOM ocean waters. B) The relationship between the zero salinity CDOM concentration estimated from buoy measurements and the DOC measured in the Lamprey River. 80% of the variability in the zero salinity CDOM estimates was explained by the river DOC when the CDOM estimates were time lagged by one day (CDOM = 13.5(±2.7) DOC + 12.8(± 17.8), N=28, $p<0.001$, dashed line). The intercept was not significantly different from zero giving CDOM = 15.4(±0.8) DOC when regression forced through zero (solid line).

There appeared to be significant differences in the input of CDOM into Great Bay as evidenced by a plot of the fluorometric CDOM concentration and salinity from the buoy (Figure 8.6 A). The daily zero salinity CDOM was estimated by linear regression of the fluorometric CDOM measurements and salinity. The zero salinity estimates were filtered to select for higher flow (flow > 316 cfs) conditions, a greater amount of variability explained by regression ($r^2>0.70$), and estimates separated from a DOC measurement by less than one day. For these conditions there were 28 pairs of data between the summers of 2005 and 2007 with 76% of the variability in the zero salinity CDOM estimates explained by the Lamprey river DOC. The variability explained increased to 80% when the CDOM estimates were time lagged by one day (Figure 8.6 B, CDOM = 13.5(±2.7) DOC + 12.8(± 17.8), N=28, $p<0.001$). The intercept was not significantly different from zero giving CDOM = 15.4(±0.8) DOC when regression forced through zero.

8.1.2 Turbidity, river discharge, and wind resuspension

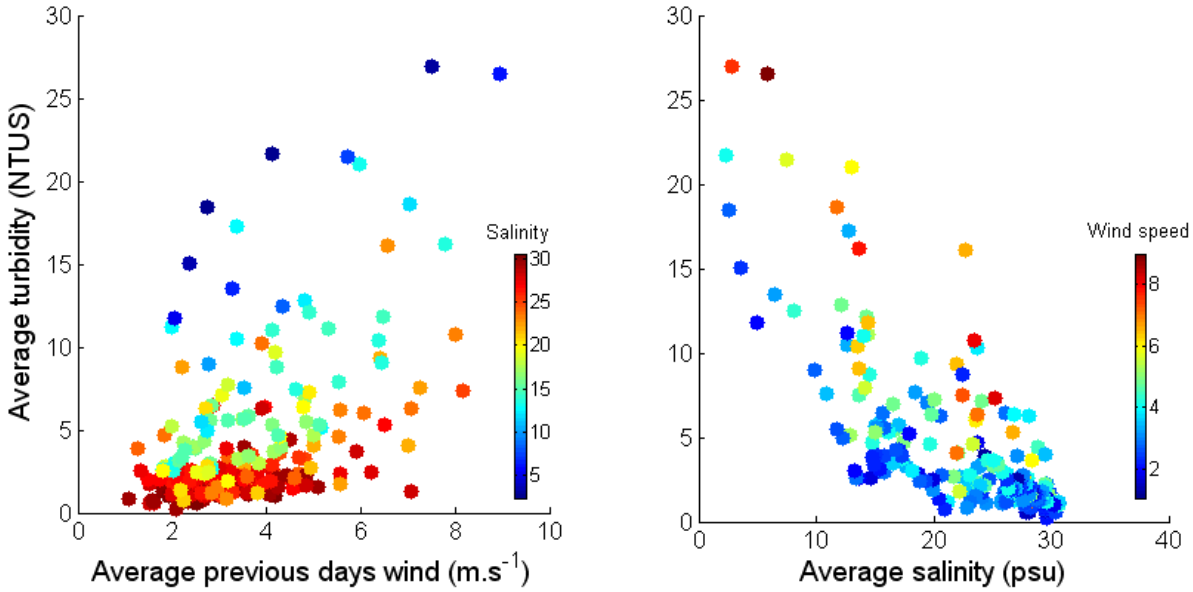

Figure 8.7 The effects of (A) windspeed and (B) river discharge (as indicated by salinity measured at the buoy) on turbidity.

High turbidity levels appeared to have occurred after high wind events (Figure 8.1) and were also associated increased river flow. A simple model for turbidity levels was that the mean daily turbidity was dependent on the mean daily wind speed for the previous day and the current daily river discharge (Figure 8.7). Salinity at the buoy was used as a proxy for the effect of discharge. 70 percent of the variability of the log transformed turbidity (NTU) was explained by the previous day's windspeed (U_w) and the current day salinity (Sal, Equation 8.2).

$$\ln(NTU) = -0.7825 + 0.1534.U_w + 0.0936.(35 - Sal) \qquad (8.1)$$

The intercept of this relationship is equivalent to a turbidity of 0.46 NTU. This relationship is not necessarily intended to predict turbidity from salinity and windspeed measurements, rather to illustrate the connectivity between turbidity and two driving forces. It confirms previous observations of increased turbidity levels under similar conditions with highest turbidity levels associated with high wind and discharge events (Ward and Bub 2005).

8.1.3 Phytoplankton and nitrate

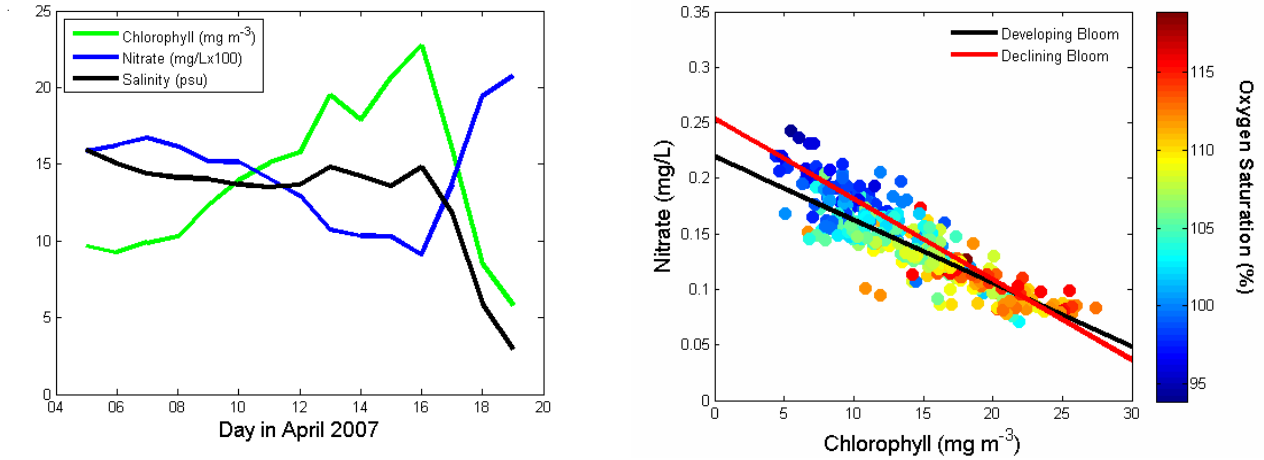

Figure 8.7 A) Time-series plot of daily averaged salinity, chlorophyll and nitrate values during a bloom event in April 2007 depicting nitrate utilization as chlorophyll concentration increases. Salinity levels remained fairly constant until significant rainfall occurs on April 16. The bloom was diluted by fresh, nutrient rich water. B) Nitrate concentrations plotted against chlorophyll values with regression lines for both developing and declining bloom activity. Oxygen saturation levels are shown by data point color; higher saturations were associated with greater chlorophyll concentrations indicative of higher photosynthetic rates.

In 2007, the Buoy was deployed on April 4th, prior to a maximum of a phytoplankton bloom which peaked on April 17th. Time-series plots of daily averaged nitrate, salinity and chlorophyll (Figure 8.7 A) showed chlorophyll concentrations more than doubled while nitrate levels fell by more than a third as salinity levels varied little during this bloom period. For the developing bloom, the regression line of nitrate vs. chlorophyll was $[NO_3^-] = -0.00570\ [Chl] + 0.220$, $r^2 = 0.71$ (Figure 8.7 B). A storm and associated heavy rainfall occurred on April 16 which resulted in a rapid decrease in salinity and chlorophyll concentration, presumably as the bloom was diluted. Nitrate concentrations increased with the influx of fresh water ($[NO_3^-] = -0.00983\ [S] + 0.246$, $r^2 = 0.92$) indicative of a freshwater nitrate concentration of 0.246 mg/L. Higher chlorophyll concentrations were associated with oxygen supersaturation (Figure 8.7 B), consistent with higher photosynthesis rates, and coincident oxygen production, which are expected with greater chlorophyll concentrations.

8.2 Observations on days of hyperspectral imagery

The two hyperspectral missions were flown with replicate 8 lines of data collection oriented approximately north-south. On August 29 the center time for the central line over Great Bay of 0857 local (1257 GMT) and on October 17 the center time for the same line was 1411 local (1811 GMT). Conditions on August 29 were near perfect with nearly cloud free skies and a low tide at the Squamscott Railroad Bridge predicted for 0849. The plan to coincide the second mission in October with the time of high tide was complicated by availability of the aircraft and sensor. A compromise of the time for low tide of 1203 on October 17 was chosen. Unfortunately heavily overcast conditions at the departure airport delayed the hyperspectral flight approximately two hours. The weather conditions were not quite as perfect as the previous collection period with some clouds apparent.

8.2.1 Time-series observations

Observations from the buoy and the USGS stream gage in the Lamprey River suggested that the goal of collecting hyperspectral imagery associated with differing flow regimes for the estuary was successfully achieved. Mean daily flow on August 29 was 0.25 m^3s^{-1} compared to 1.87 m^3s^{-1} on October 17. This represented greater than a seven fold increase in flow between the two sampling periods (Figure 8.8A). Shorter term temporal variability was evident in the water quality and clarity observations at the buoy. The semi-diurnal tide meant that warmer-fresher water and colder-saltier water were alternately experienced at the buoy at successive low and high tides, respectively, at the end of August (Figure 8.8B). Higher CDOM levels were associated with fresher periods as were periods of increased turbidity. Interestingly the timings of maximal CDOM and turbidity levels were offset with highest turbidity levels occurring 30 to 60 minutes prior to maximal CDOM levels. A potential explanation for this observation is the inclusion of more turbid waters draining from shallow mud flats immediately before low water (as indicated by lowest salinity). Chlorophyll-a concentrations, as indicated by the fluorometer on the buoy, also varied with the state of the tide with higher values associated with higher salinities. In general midday values of these chlorophyll maxima were smaller that those at night probably due to non-photochemical quenching effects (Morrison 2003). Diffuse downwelling attenuation closely followed the trends noticed in the CDOM and turbidity and on the day of the overflight increased to a high of 1.11 m^{-1} at 0833 then decreased steadily for the rest of the day. On October 17 the reverse relationship between salinity and water temperature was seen compared to August (Figure 8.8C). Higher water temperatures were associated with higher salinity waters, at least initially. CDOM and turbidity again showed an inverse correlation with salinity, generally decreased over three days enveloping the overflight day, and the diffuse attenuation coefficient closely tracked the turbidity and CDOM concentration.

A)

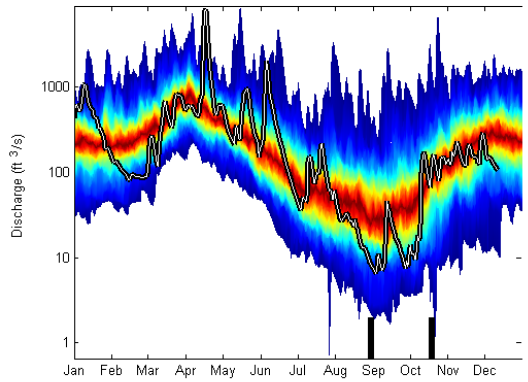

Figure 8.8 Daily mean discharge from the Lamprey River measured at the USGS stream gage station (#01073500). The color gradient represents the statistical range of observations since gage initiation in 1934. The two days of the hyperspectral overflight are marked with back bars at the bottom of the figure. The discharge on the August 29, 2007 was 0.25 m^3s^{-1} compared to 1.87 m^3s^{-1} on October 17. On August 29 the observed K_d(PAR) at the time of the HS imagery collection (0854 local) was 0.92 m^{-1} with a D_o of 1.29 yielding an effective K_d(PAR) of 0.71 m^{-1}.

B) August 29, 2007

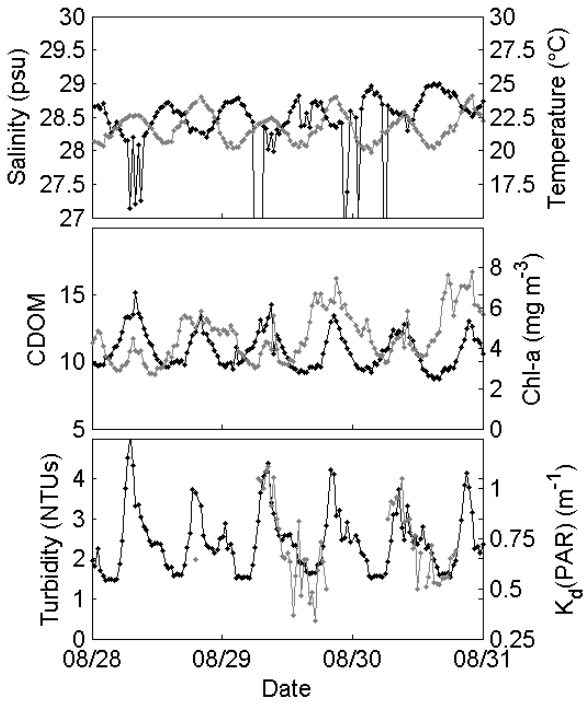

C) October 17, 2007

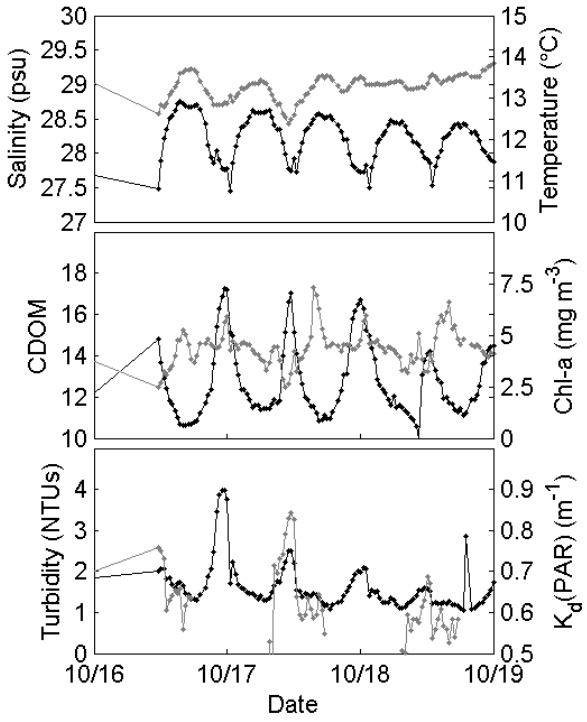

8.2.2 Continuous along-track sampling

8.2.2.1 August 29, 2007

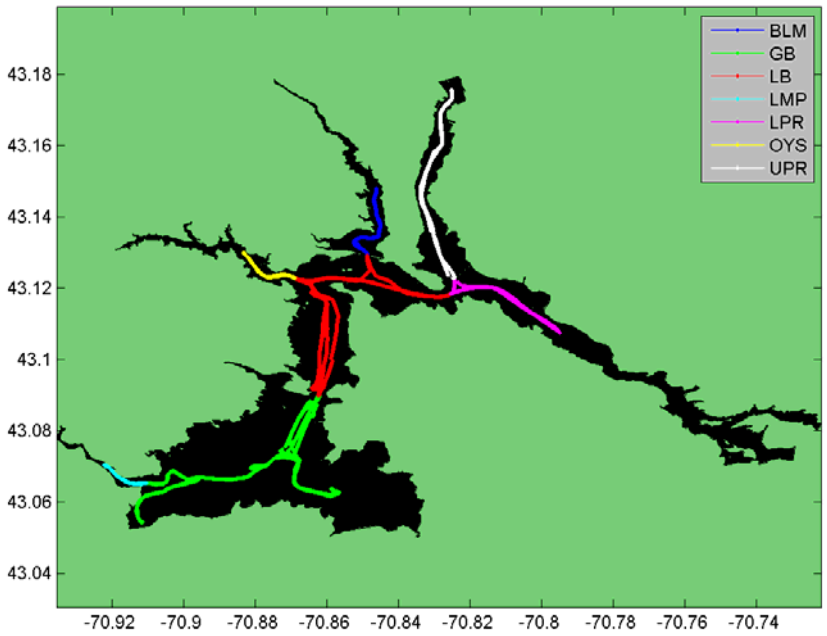

Figure 8.9 Trace of along track measurements on August 29, 2007. The sampling covered 7 of the NHEP estuarine sampling areas.

Along-track measurements highlighted the spatial and temporal variability associated with estuarine environment. On August 29th seven NHEP estuarine assessment zones were visited (Figure 8.9) in the space of 4 hours and 10 minutes. The mean daily flow in the Lamprey River was 0.25 m^3s^{-1}. The coldest most saline water was found in the lower Piscataqua river, while the warmest and freshest water was found in the Lamprey River (Figures 8.10 and 8.11 A and B). The spatial variability of the three main optical constituents generally showed higher values in the tributaries especially CDOM and chlorophyll-a (Figures 8.10 and 8.11 C and D). Comparison with the grab sample values of chlorophyll-a indicated that the along-track fluorometer chlorophyll-a values were higher than the grab samples by a factor of 1.66. Consequently the along-track chlorophyll-a values were scaled with this factor. The variability in turbidity was not as marked. The beam attenuation was used as a proxy for turbidity which was normally dominated by non-algal particulates (Figures 8.10 and 8.11 E and F). Comparison of the data from the transmissometer in the core along-track measurement suite and the ac-9 highlighted some of the difficulties in combining data from multiple instruments with differing flow paths. Discrepancies between the two instruments in the Great Bay and Lamprey River assessment areas were apparent indicative of a potential partial obstruction of the ac-9 flow stream. This smeared the ac-9 data and a feature matching procedure was implemented whereby clearly discernable maxima and minima in the two data streams were aligned. As mentioned above, the overflight and the in situ sampling encompassed the 0849 time of low water at the Squamscott railroad bridge. As such, the along-track measurements sampled not only the spatial variability but also temporal variability. This was most pronounced in the southern assessment areas where there were marked changes between observations made going upstream and downstream in the tributaries.

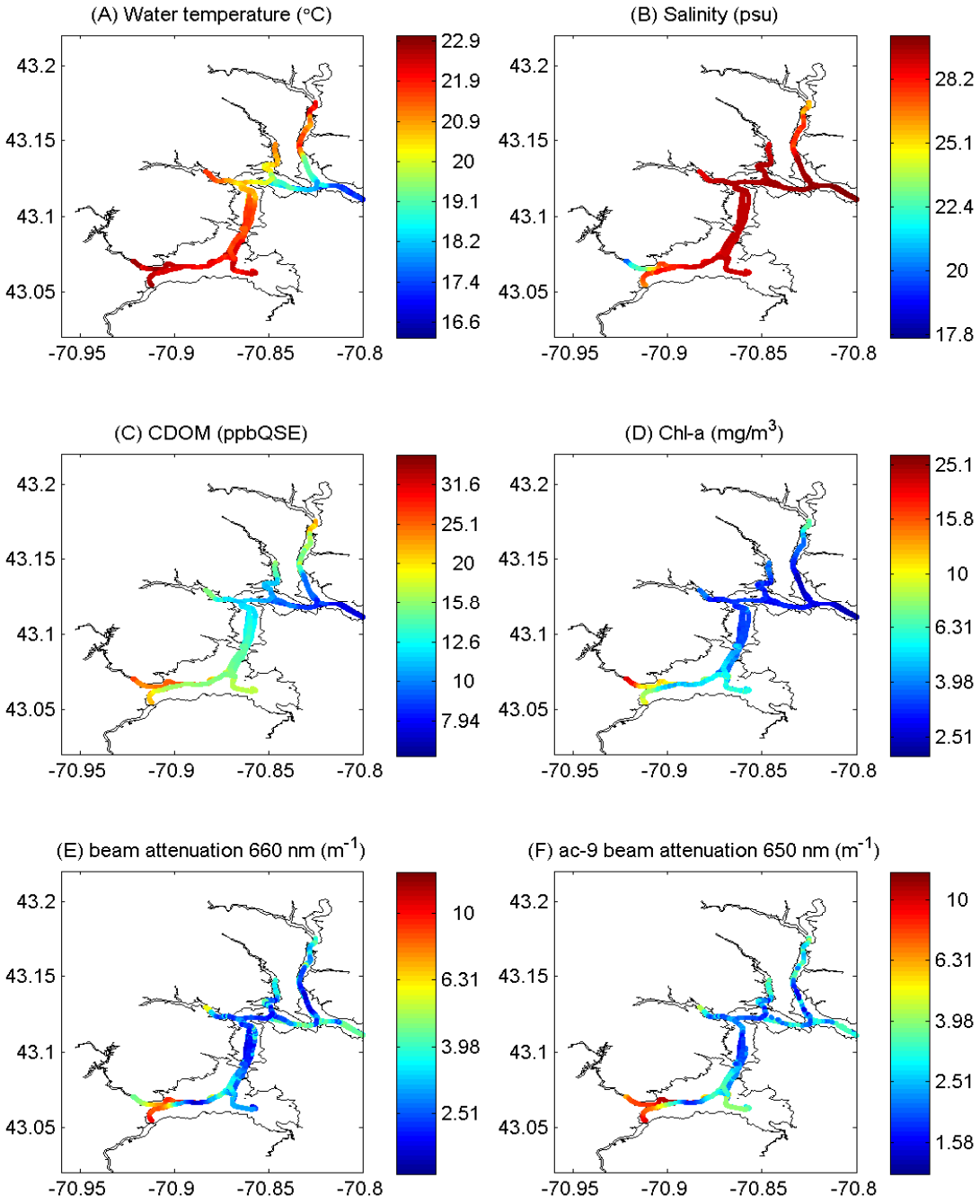

Figure 8.10 Graphical representation of the spatial variability in water quality parameters observed with continuous along-track sampling on August 29, 2007. A and B) Warmer fresher waters were found in the tributaries which were often associated with higher CDOM (C) and chlorophyll-a concentrations (D). The bottom two panels represent beam attenuation measurements from two different instruments; E) the transmissometer as part of the core along-track measurement suite, and F) the ancillary ac-9. Observations with the two instruments were similar north of Adams Point; however there was an apparent difference between the two units south of Adams Point that was especially noticeable in the Lamprey River.

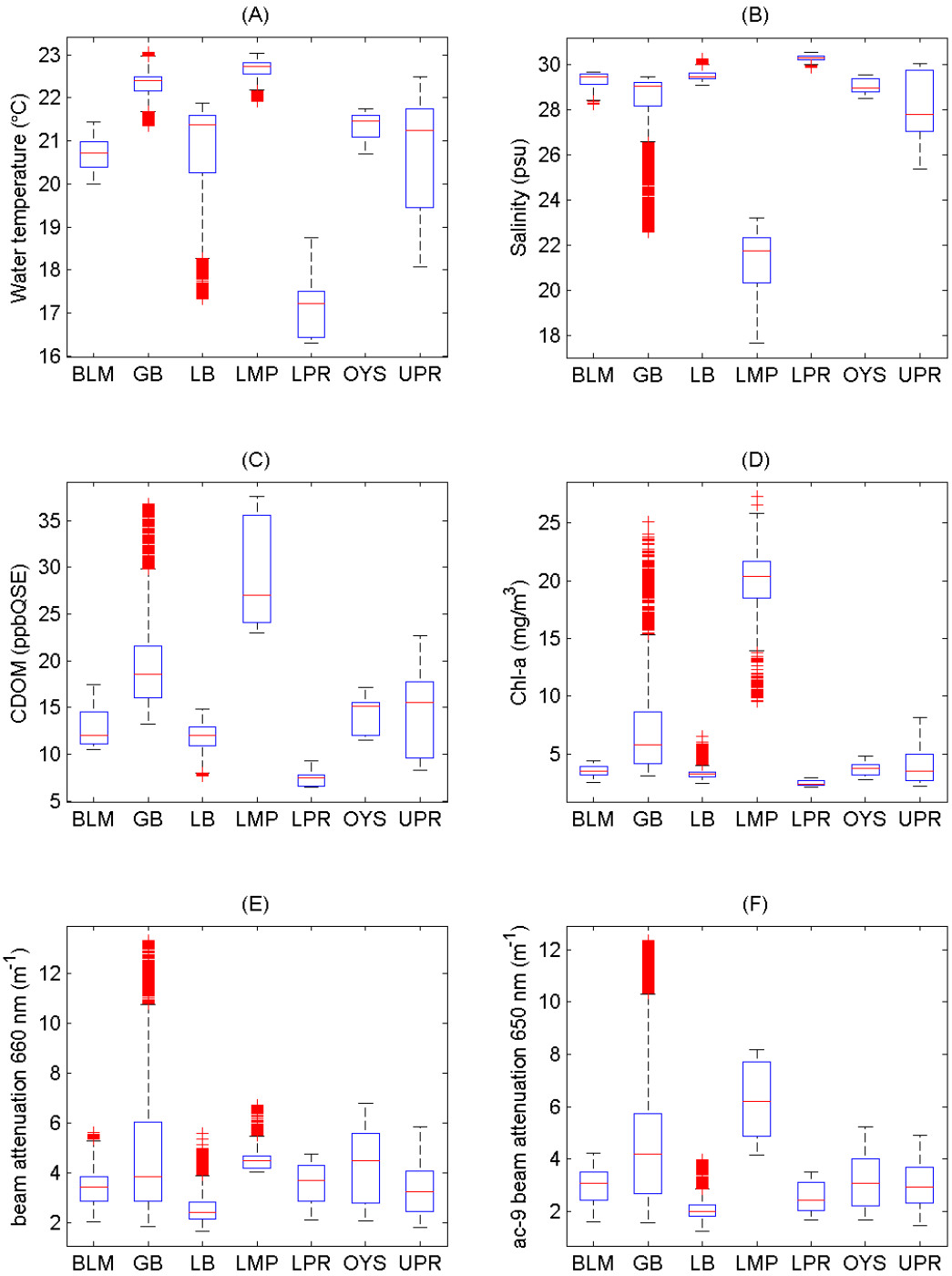

Figure 8.11 Box and whisker plots representing the statistical distribution of water quality parameters observed for each of the seven NHEP estuarine assessment areas visited during August 29, 2007. The six panels correspond to the spatial variability panels in the previous Figure (8.9). Each box has lines at the lower quartile, median, and upper quartile values. The whiskers are lines extending from each end of the box to show the extent of the rest of the data. Outliers are data with values beyond the ends of the whiskers. If there is no data outside the whisker, a dot is placed at the bottom whisker. The difference in the two estimates of the beam attenuation coefficient is noticeable in panels E and F where the ac-9 estimate in the Lamprey River is elevated. Summary data for each assessment zone are available in the Appendices.

K_d(PAR) was estimated in two ways from the continuous along-track data-stream. The absorption and beam attenuation observations from the ac-9 facilitated calculation of and apparent K_d(PAR) from Equation 8.1. For this an estimate of the back scattering ratio is necessary and the value of 0.0215 calculated from IOP profiler measurements in Great Bay on the day of the over flight. Alternatively, the multivariate model derived from the buoy observations (Equation 8.1) can be used with along-track measurements. For this a conversion of the beam attenuation at 660 nm to turbidity (NTU) is necessary. The ac-9 measurements were used to derive a relationship between $c_{nw}(650)$ and $b_{nw}(715)$ [$c_{nw}(650) = 1.075.b_{nw}(715) + 0.979$, $r^2 = 0.99$].

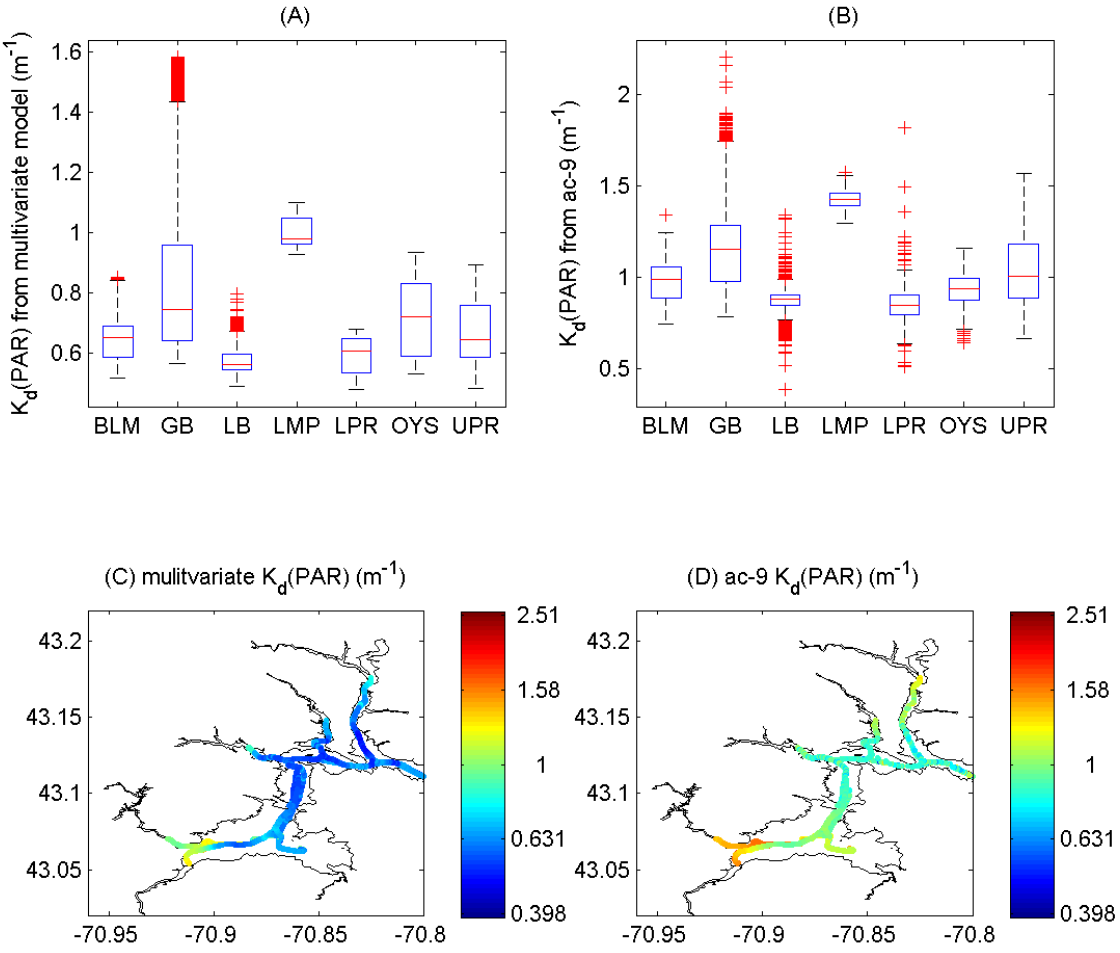

Figure 8.12 Apparent PAR diffuse attenuation coefficients, K_d(PAR) calculated with continuous along track sampling observations. Box and whisker plots, A) from the ac-9 spectral measurements of absorption and attenuation, and B) with the multivariate model of Equation 3 parameterized for the available along-track measurements. C) Graphical representation of the spatial distribution of the K_d(PAR) from the multivariate model.

8.2.2.2 October 17, 2007

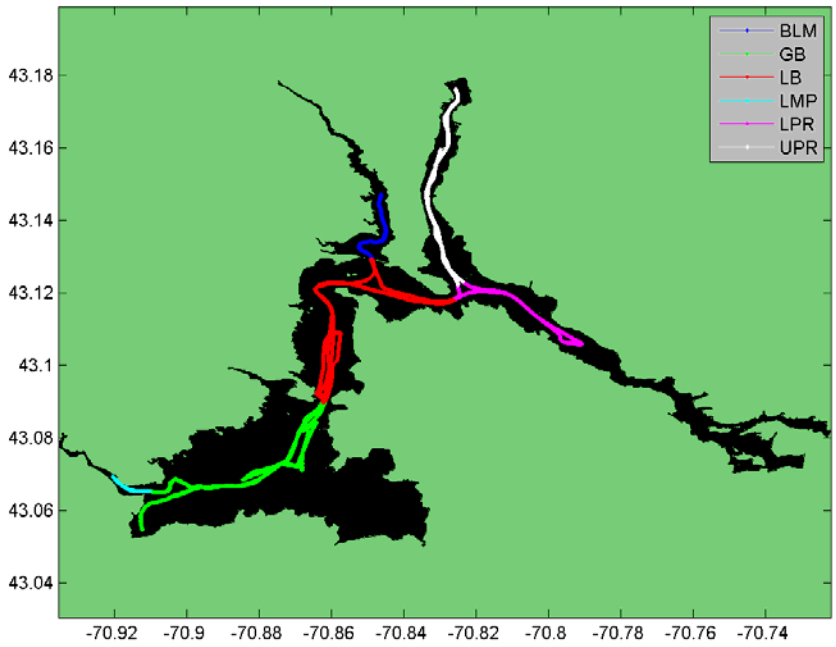

Figure 8.13 Trace of along track measurements on October 17, 2007. The sampling covered 6 of the NHEP estuarine sampling areas.

Along-track sampling on the R/V Galen J visited six of the NHEP estuarine assessment areas between 11:10 and 15:32 on October 17, 2007 (Figure 8.13). On this day the Oyster River was not sampled in comparison to the August field measurements. The mean daily flow in the Lamprey River was 1.87 m^3s^{-1} which was 7.4 times greater than the flow in August. In general water temperatures were lower and the amount of freshwater greater (Figures 8.14 and 8.15 A and B). The increased discharge was also associated with increased levels of CDOM (Figures 8.14 and 8.15 C) but chlorophyll concentrations were lower (Figures 8.14 and 8.15 D).

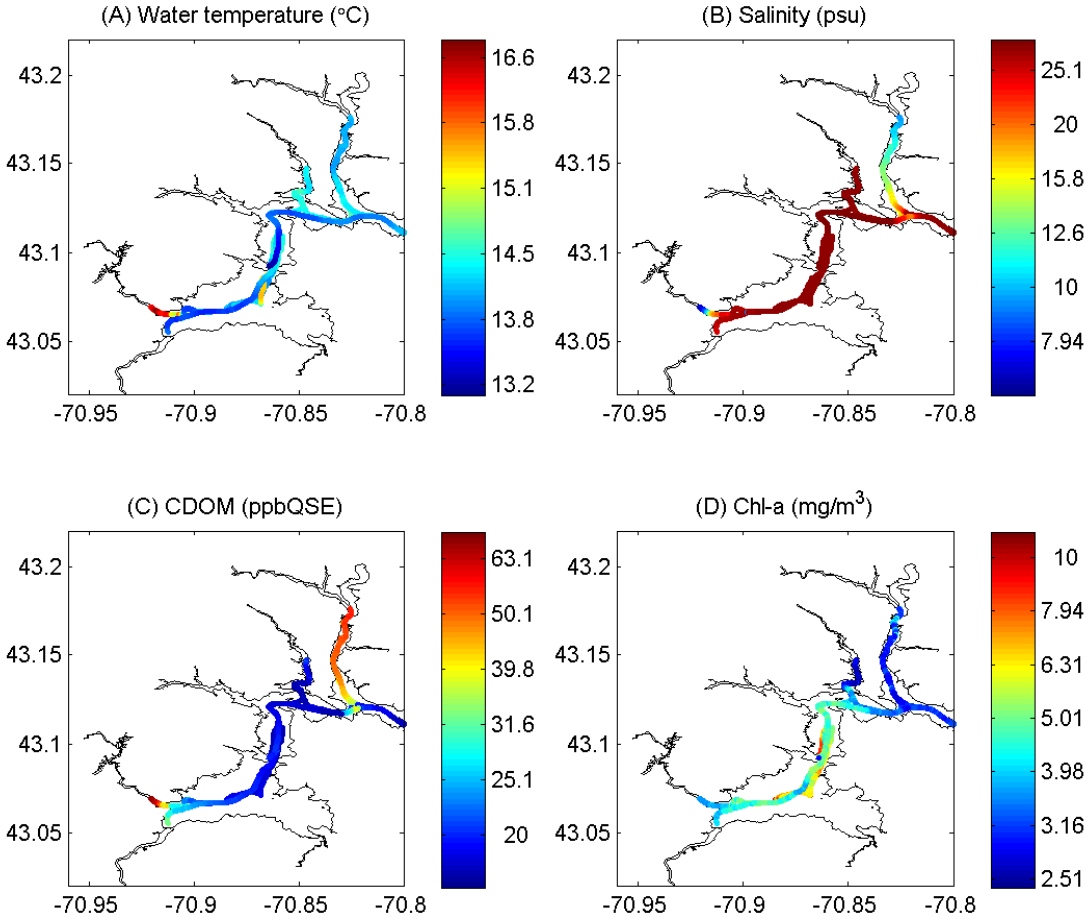

Figure 8.14 Graphical representation of the spatial variability in water quality parameters observed with continuous along-track sampling on October 17, 2007. A) Water temperature varied throughout the sampling period and was highest in the Lamprey River. B) Lower salinities were found in the Lamprey and Upper Piscataqua Rivers and were associated with higher CDOM concentrations (C). (D) Highest chlorophyll-a concentrations were found in Great and Little Bays.

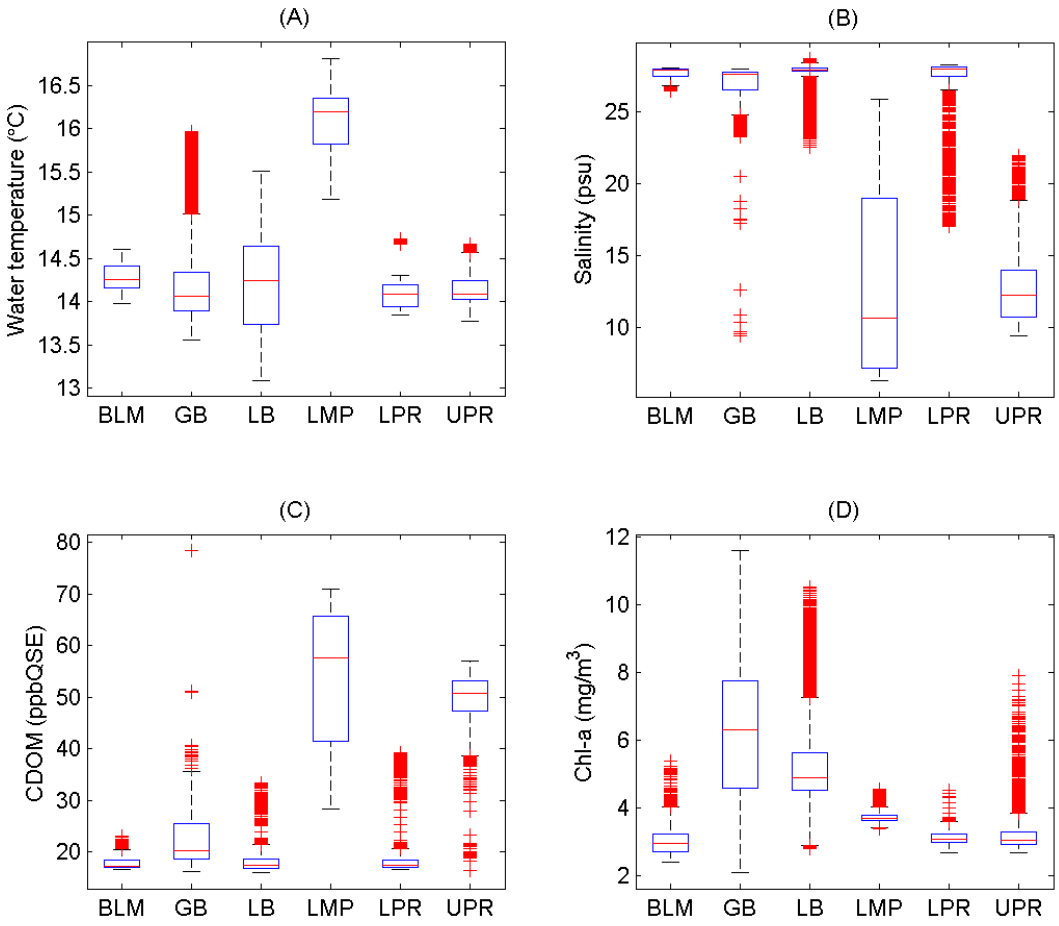

Figure 8.15 Box and whisker plots representing the statistical distribution of water quality parameters observed for each of the six NHEP estuarine assessment areas visited during October 17, 2007. The four panels correspond to the spatial variability panels in the previous Figure (8.14). Each box has lines at the lower quartile, median, and upper quartile values. The whiskers are lines extending from each end of the box to show the extent of the rest of the data. Outliers are data with values beyond the ends of the whiskers. If there is no data outside the whisker, a dot is placed at the bottom whisker. Summary data for each assessment zone are available in the Appendices.

8.2.3 Grab samples

Grab sample data for both August 29, 2007 and October 17, 2007 are summarized in Table 8.2 A range of values for chlorophyll, total suspended material (TSS), CDOM and the nutrients nitrate + nitrite and phosphate were seen on both days. In August, chlorophyll and nitrate + nitrate concentrations in riverine samples were, in many cases, more than an order of magnitude greater than samples from stations in open waters of Little Bay and Great Bay. Highest values for chlorophyll and nitrate + nitrite were in the Cocheco River (NH-0058A). The chlorophyll concentration at this station was twice as great as the next highest (GRBCL, Chapman's Landing) and it's important to mention that duckweed was present at the Cocheco station. Phosphate values were less dependent on station type than other parameters: both the highest (GRBOR, Oyster River) and the lowest (NH-0062A, Salmon Falls River) concentrations were found in riverine samples. Bay phosphate levels were more moderate and consistent. Total suspended material and CDOM values were generally greater in riverine samples although the disparity is less marked than with nitrate + nitrite and chlorophyll.

In October, the large range of chlorophyll values was not present due to generally much lower values in the tributaries. While the median chlorophyll value was similar for both sampling days, the %RSD for chlorophyll on each day was quite different (149% in August and 44% in October). The highest chlorophyll value was found adjacent to the Great Bay Coastal Buoy while the lowest chlorophyll concentration was seen in the Cocheco River (NH-0058A). Interestingly, the Cocheco River station had exhibited the highest chlorophyll signal in August. Again, large ranges in nitrate + nitrate concentrations were apparent and followed the pattern seen in August but with higher values throughout the system; once again some riverine samples were an order of magnitude higher than bay samples. The highest nitrate + nitrite value was in the Oyster River (GRBOR) while the lowest was in center of Great Bay (GB4A). Phosphate values were similar to patterns seen in August. Both high and low phosphate values were seen at the same stations as in August (Oyster River and Salmon Falls River, respectively). Bay samples were generally slightly depleted in phosphate compared to August; this trend is the opposite as that seen for nitrate + nitrite. Suspended material signals for October in bay samples were similar to August levels while river samples were, on the whole, less turbid than in August. Greater variability in CDOM was seen this month. While bay samples were similar to August, many riverine samples showed higher absorption than in August.

Table 8.2 Grab Sample Data Summary

Sample ID	Time (EDT)	Chl (mg m^{-3})	TSM (g/L)	ag_{440} (m^{-1})	$NO_2^- + NO_3^-$ (mg/L)	PO_4^{3-} (mg/L)	K_d(PAR) (m^{-1})
GB4A	8/29/07 8:30	7.08	0.03725	0.7772	0.013	0.068	2.100
GRBAP	8/29/07 7:59	2.99	0.00630	-9999	0.014	0.059	1.164
GRBAP	8/29/07 9:34	3.66	0.01240	0.4756	0.013	0.044	-9999
GRBAP	8/29/07 9:34	3.26	0.00915	0.4962	0.011	0.055	-9999
GRBAP	8/29/07 9:34	3.18	0.00865	0.4902	0.014	0.046	-9999
GRBCL	8/29/07 8:46	49.05	0.03320	1.6282	0.145	0.047	4.362
GRBGB	8/29/07 8:12	3.59	0.01520	0.5993	0.009	0.067	0.955
GRBGB	8/29/07 8:40	3.82	0.00605	0.7232	0.005	0.054	1.130
GRBLR	8/29/07 7:35	23.58	0.00480	1.5857	0.094	0.039	1.482
GRBOR	8/29/07 7:04	8.82	0.01755	1.1415	0.228	0.135	2.301
GRBSF	8/29/07 9:05	33.09	0.00725	2.0045	0.071	0.030	-9999
GRBSQ	8/29/07 8:29	35.37	0.08770	1.1436	0.061	0.060	6.425
NH00-0027B	8/29/07 8:54	3.34	0.01345	0.7429	0.008	0.065	-9999
NH-0049A	8/29/07 9:34	5.12	0.00600	0.6833	0.088	0.076	0.885
NH-0052A	8/29/07 9:20	5.56	0.00570	0.6606	0.012	0.050	0.929
NH-0057A	8/29/07 8:20	10.75	0.00370	1.2739	0.010	0.029	-9999
NH-0058A	8/29/07 8:37	98.11	0.01200	1.5044	1.081	0.059	-9999
NH-0062A	8/29/07 8:55	20.41	0.00700	1.6029	0.008	0.014	-9999
NH04-235C	8/29/07 9:14	3.49	0.00565	0.6833	0.006	0.040	-9999
NH04-245C	8/29/07 9:33	3.15	0.00615	0.5212	0.013	0.043	-9999
NH04-245C	8/29/07 9:33	2.63	0.00545	0.5401	0.010	0.041	-9999
NH04-245C	8/29/07 9:33	2.79	0.00725	0.7035	0.015	0.044	-9999
	Mean	**15.13**	**0.0144**	**0.9515**	**0.088**	**0.053**	
	Median	**4.47**	**0.0073**	**0.72**	**0.013**	**0.049**	
	%RSD	**149.43**	**128.1**	**49.3**	**260.9**	**43.9**	
GB4A	10/17/07 14:37	4.33	0.00700	0.4595	0.041	0.030	-9999
GRBAP	10/17/07 13:47	3.64	0.00760	0.4371	0.073	0.042	0.674
GRBAP	10/17/07 15:34	3.83	0.00555	0.5491	0.065	0.042	-9999
GRBCL	10/17/07 13:17	4.27	0.01112	1.3236	0.471	0.087	1.417
GRBGB	10/17/07 13:57	5.37	0.00630	0.5535	0.045	0.034	0.612
GRBGB	10/17/07 14:33	6.14	0.00720	0.5349	0.049	0.033	0.650
GRBLR	10/17/07 13:27	1.81	0.00485	2.8685	0.112	0.018	1.335
GRBOR	10/17/07 12:32	4.99	0.00865	0.7527	1.684	0.410	1.031
GRBSF	10/17/07 12:55	1.67	0.00190	2.7309	0.124	0.013	-9999
GRBSQ	10/17/07 12:55	2.27	0.00780	1.1057	0.267	0.067	0.828
NH-0049A	10/17/07 14:09	4.38	0.00590	0.5321	0.072	0.037	0.633
NH-0052A	10/17/07 14:20	2.84	0.00580	0.5675	0.076	0.044	0.578
NH-0057A	10/17/07 13:10	1.41	0.00510	1.3765	0.288	0.041	-9999
NH-0058A	10/17/07 12:30	0.93	0.00400	2.7585	0.863	0.045	-9999
NH-0062A	10/17/07 12:47	1.77	0.00705	2.0315	0.157	0.010	-9999
NH04-235C	10/17/07 14:56	6.12	0.00645	0.4408	0.058	0.039	0.580
NH04-245C	10/17/07 15:18	4.47	0.00615	0.4914	0.067	0.043	0.610
NH04-245C	10/17/07 15:18	4.05	0.00610	0.4986	0.070	0.035	0.610
NH04-245C	10/17/07 15:18	4.60	0.00740	-9999	0.078	0.035	0.610
	Mean	**3.62**	**0.0064**	**1.11**	**0.245**	**0.058**	
	Median	**4.05**	**0.0063**	**0.56**	**0.076**	**0.039**	
	%RSD	**44.1**	**29.5**	**79.2**	**164.0**	**149.2**	

Analytical precision for grab samples field replicates is given in Table 8.3. Two field triplicates were taken in August and one was sampled in October. Percent relative standard deviation (%RSD) for chlorophyll triplicates were <10%, TSS triplicates were <21%, CDOM a_g440 triplicates were <18%, nitrate + nitrite triplicates were <19% and phosphate triplicates were<13%. Acceptable precision for field replicates indicates the validity of the grab samples on both Aug. 29 and Oct. 17.

Table 8.3 Grab Sample Analytical Precision

Sample Date	Sample ID	Chl (mg m^{-3})	TSM (g/L)	ag_{440} (m^{-1})	$NO_2^-+NO_3^-$ (mg/L)	PO_4^{3-} (mg/L)
20070829	GRBAP	3.66	0.01240	0.4756	0.013	0.044
20070829	GRBAP	3.26	0.00915	0.4962	0.011	0.055
20070829	GRBAP	3.18	0.00865	0.4902	0.014	0.046
Mean		**3.37**	**0.01007**	**0.4873**	**0.012**	**0.048**
%RSD		**7.7**	**20.2**	**2.2**	**11.1**	**12.4**
20070829	NH04-245C	3.15	0.00615	0.5212	0.013	0.043
20070829	NH04-245C	2.63	0.00545	0.5401	0.010	0.041
20070829	NH04-245C	2.79	0.00725	0.7035	0.015	0.044
Mean		**2.86**	**0.00628**	**0.5883**	**0.013**	**0.043**
%RSD		**9.4**	**14.4**	**17.0**	**18.3**	**4.3**
20071017	NH04-245C	4.47	0.00615	0.4914	0.067	0.043
20071017	NH04-245C	4.05	0.00610	0.4986	0.070	0.035
20071017	NH04-245C	4.60	0.00740	-9999	0.078	0.035
Mean		**4.37**	**0.00655**	**0.4950**	**0.072**	**0.038**
%RSD		**6.6**	**11.2**	**-9999**	**7.7**	**12.1**

Grab Sample K_d(PAR)

For both sampling days, equations describing the diffuse attenuation coefficient (K_d(PAR)) in terms of grab sample concentrations of chlorophyll-a, a_g(440), and TSS were derived using multiple linear regression. For August, the equation was:

$$K_d(PAR) = 0.0386[chl] + 50.42[TSS] + 0.392[ag440] + 0.0914 \quad (8.2)$$

The equation for October was:

$$K_d(PAR) = 0.0182[chl] + 100.0[TSS] + 0.390[ag440] - 0.311 \quad (8.3)$$

Correlation coefficients for August and October are quite good; r^2 values are 0.97 and 0.96, respectively. The chlorophyll specific diffuse attenuation coefficients were of the same order of magnitude as that estimated with the buoy observations (0.0188 m^2 mg^{-1}, Equation 7.2). Similarly, the TSS and the CDOM specific coefficients were of the same order of magnitude as those derived from the buoy measurements (40.0 $m^{-1}(mg/L)^{-1}$ and 0.273, respectively, when converted using factors in Table 7.3).

8.2.4 Hyperspectral imagery

8.2.4.1 Data Quality and Atmospheric correction

A variety of techniques were used to assess the quality of the remotely sensed data. The Tafkaa atmospheric correction and other methods that are detailed in Appendix 10.1 all concluded that there were large uncertainties associated with wavelengths less than approximately 550 nm. Recent communication with SpecTIR, the contractor for the aerial imagery, indicated concerns with the radiometric calibration at these blue wavelengths. Unfortunately most inversion techniques associated with determining water quality and benthic characteristics (e.g., Lee et al. 1999; Mobley et al. 2005) from remotely sensed data require blue wavelengths which are important for distinguishing the absorption associated with CDOM and phytoplankton. As such, we were unable to complete the goal of the project to determine the spatial variability of optically important constituents from the HS imagery. Instead we concentrated on determining the spatial variability in the PAR attenuation with the newly developed approach detailed in Section 7.3.4. Given the time constraints associated with funding available for the work only the overflight on August 29, 2007 was able to be analyzed.

8.2.4.2 Water quality

Twelve of the NHEP estuarine assessment areas were observed with the HS imagery on August 29, 2007 (Figure 8.17). The effective K_d(PAR) retrieved from inversion of the remote sensing reflectance varied from a minimum of 0.54 m^{-1} in Little Bay to a maximum of 5.37 m^{-1} in the Salmon Falls River (Table 8.4). This maximum was an extreme value with most values concentrated between 0.5 and 2 m^{-1} with a mean of 0.81 and standard deviation of 0.25 m^{-1}. Similar to the along-track measurements the lowest mean attenuation values were found in the Lower Piscataqua River and Little Bay. The highest mean values were associated with the tributaries with the Squamscott River having the poorest water clarity. Sampling of 625 pixels surrounding the Great Bay Coastal Buoy indicated that the effective K_d(PAR) was 0.72 (± 0.05) m^{-1} which was extremely close to that observed by sensors on the buoy of 0.71 m^{-1}. Similarly comparison with other in situ measurements showed a good agreement with the HS K_d(PAR) estimates explaining 88% of the variability (Figure 8.16). This represents a remarkable degree of consistency between the two data sets considering the high degree of spatial and temporal variability within the estuarine environment.

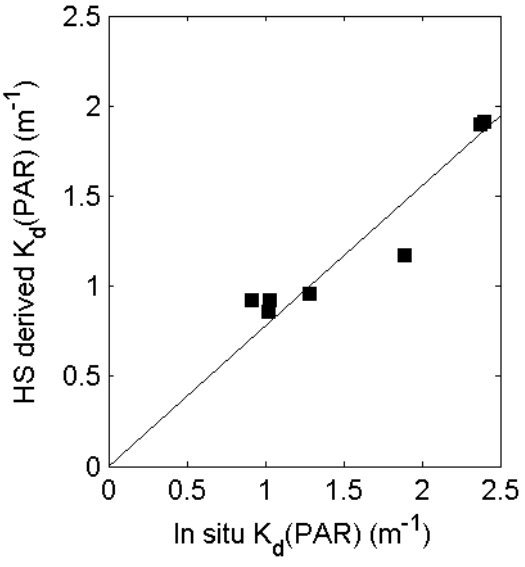

Figure 8.16 Comparison between the attenuation coefficient measured in-situ and that derived from the HS imagery. For this comparison data from GRBAP, GRBGB, GRBLR, GRBOR, collected by LeClair and GB4A, and GRBGB collected by Morrison et al. were used. Also included are the K_d(PAR) estimate from the 0900 local time at the Great Bay Coastal Buoy. Information from the Squamscott River and those collected by Edwards were excluded from this analysis as in situ measurements were either collected in close proximity to shading structures or later than other measurements. An initial linear regression analysis indicated that the intercept was not significantly different from zero giving that the HS K_d(PAR) = 0.78 in situ K_d(PAR) (r^2 = 0.88).

Assessment Zone		BLM	CCH	GB	LB	LMP	LPR	NMP	OYS	SFR	SQM	Spinney	UPR
Number		282872	114945	2729484	1181525	70600	695926	50993	208838	236631	116069	82745	526272
K_d(PAR)	Min	0.70	1.10	0.57	0.54	1.08	0.50	0.74	0.59	1.00	1.27	0.87	0.60
	Max	1.10	1.88	3.12	2.89	2.31	2.30	1.22	3.13	5.37	2.68	1.22	1.96
	Mean	**0.84**	**1.29**	**0.86**	**0.69**	**1.43**	**0.71**	**0.96**	**1.01**	**1.34**	**1.79**	**1.08**	**0.94**
	Stdev	0.06	0.09	0.24	0.08	0.20	0.10	0.11	0.29	0.24	0.12	0.07	0.15
Turbidity	Min	3.112	1.413	1.596	0.423	1.504	0.423	4.001	2.249	1.049	2.249	0.958	1.230
	Max	5.974	5.653	58.241	15.599	26.024	28.221	14.313	44.571	6.406	32.553	8.787	6.298
	Mean	**4.202**	**4.323**	**4.453**	**2.695**	**6.628**	**2.511**	**6.931**	**6.393**	**3.618**	**11.803**	**3.865**	**3.096**
	Stdev	0.535	0.510	2.221	0.699	1.926	0.954	1.414	2.679	0.654	0.914	0.418	0.594
b_b(555)/a(555)	Min	0.147	0.032	0.096	0.027	0.034	0.019	0.129	0.065	0.007	0.049	0.029	0.042
	Max	0.337	0.147	1.650	0.898	0.641	3.487	0.976	1.453	0.132	0.773	0.315	0.200
	Mean	**0.238**	**0.123**	**0.237**	**0.203**	**0.170**	**0.179**	**0.351**	**0.283**	**0.098**	**0.247**	**0.138**	**0.140**
	Stdev	0.011	0.016	0.034	0.032	0.036	0.030	0.051	0.032	0.016	0.021	0.010	0.016
a(555)	Min	0.342	0.729	0.244	0.222	0.651	0.192	0.288	0.262	0.665	0.854	0.544	0.271
	Max	0.729	1.589	2.113	2.519	1.795	1.911	0.847	2.034	5.213	1.828	0.910	1.566
	Mean	**0.460**	**0.924**	**0.478**	**0.349**	**1.010**	**0.361**	**0.516**	**0.588**	**0.990**	**1.244**	**0.740**	**0.589**
	Stdev	0.051	0.092	0.187	0.066	0.169	0.081	0.086	0.226	0.239	0.114	0.063	0.146

Table 8.4 Summary of water quality parameters derived with hyperspectral imagery from August 29, 2007.

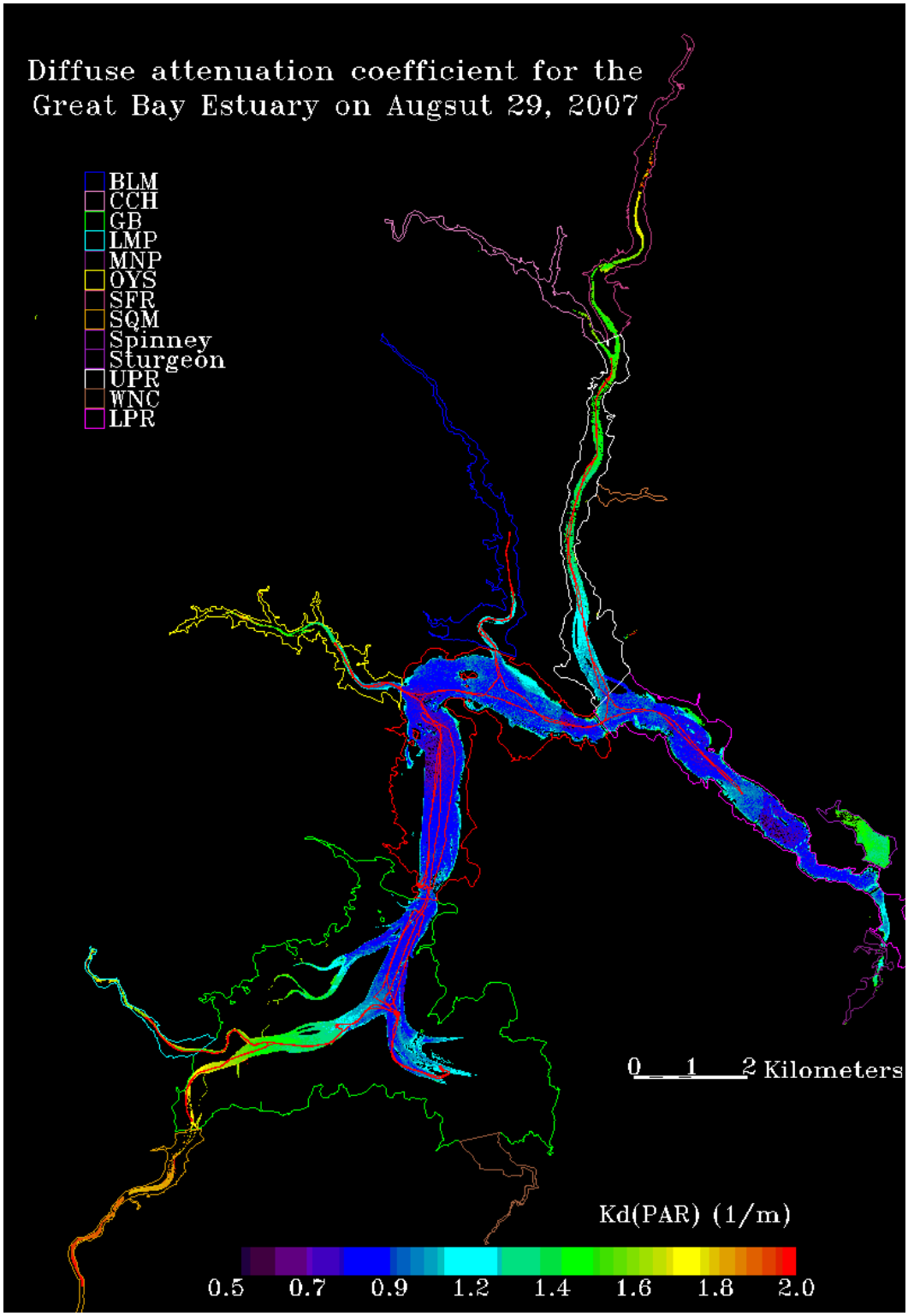

Figure 8.17 Remotely sensed effective PAR diffuse attenuation coefficient, K_d(PAR),for optically deep waters from the HS imagery collected on August 29, 2007. Outlines of the NHEP estuarine assessment zones are given as is the transect of the along-track measurements in red.

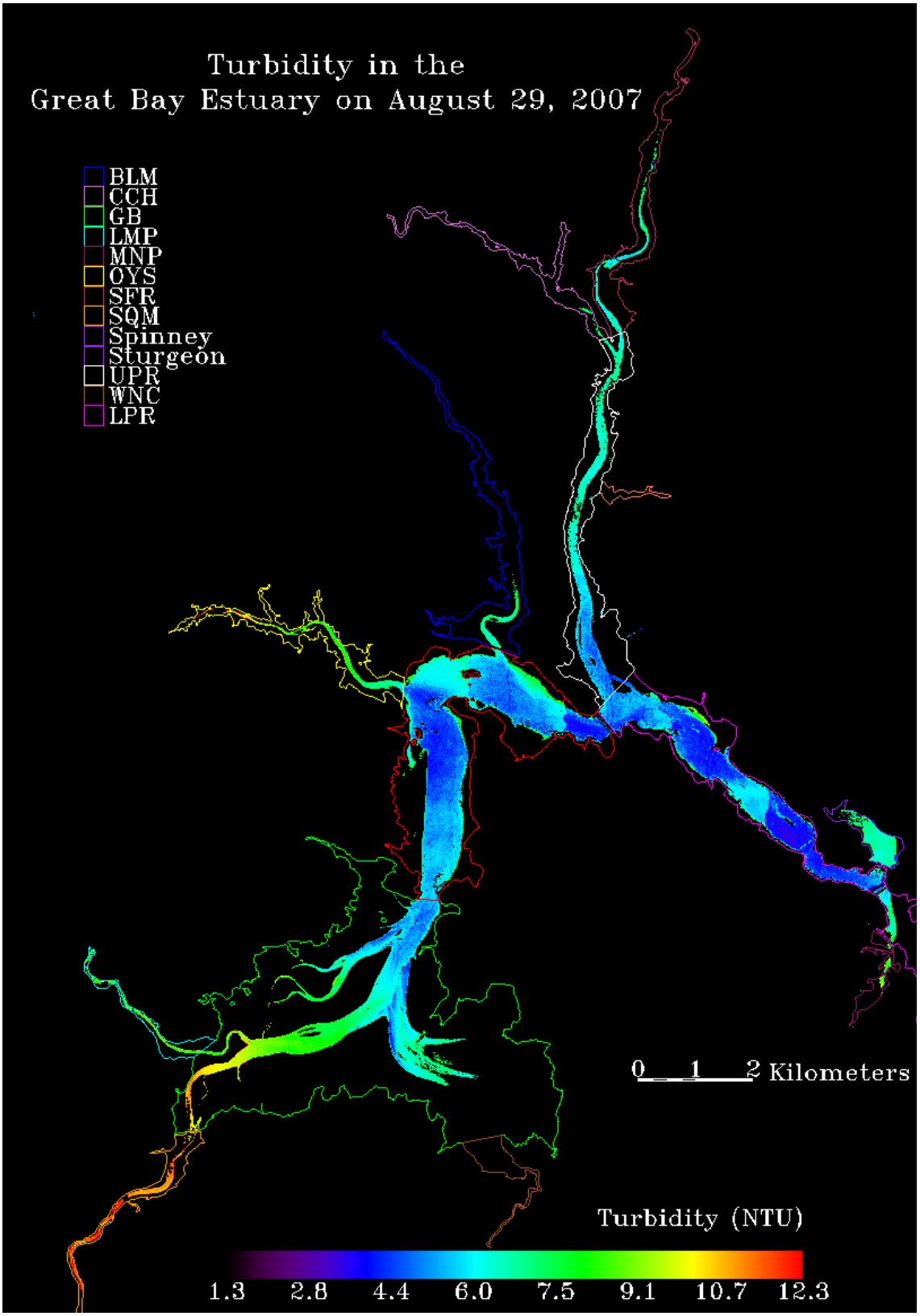

Figure 8.18 Remotely sensed turbidity in the Great Bay Estuary on August 29, 2007. Outlines of the NHEP estuarine assessment zones are given.

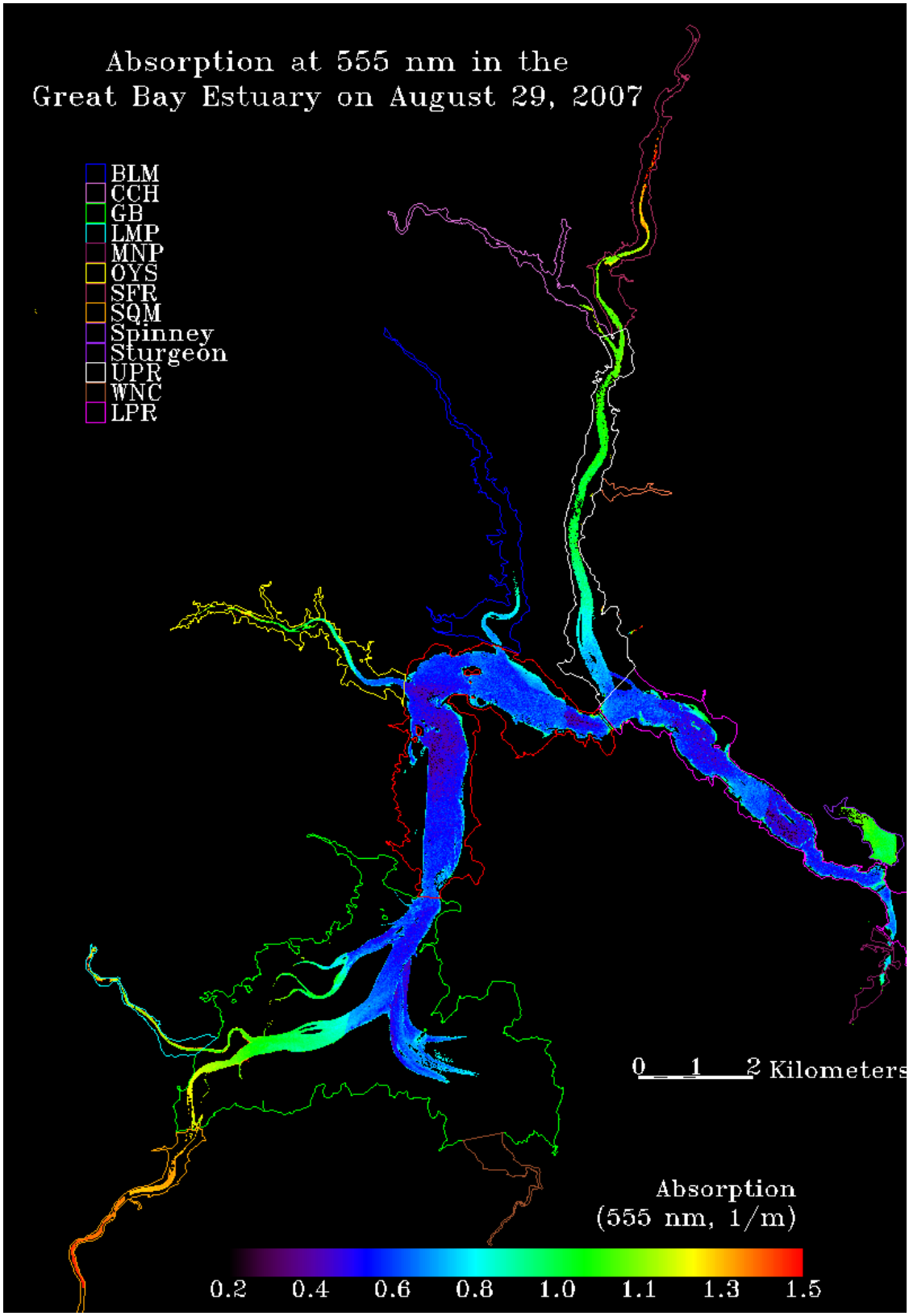

Figure 8.19 Remotely sensed absorption at 555 nm in the Great Bay Estuary on August 29, 2007. Outlines of the NHEP estuarine assessment zones are given.

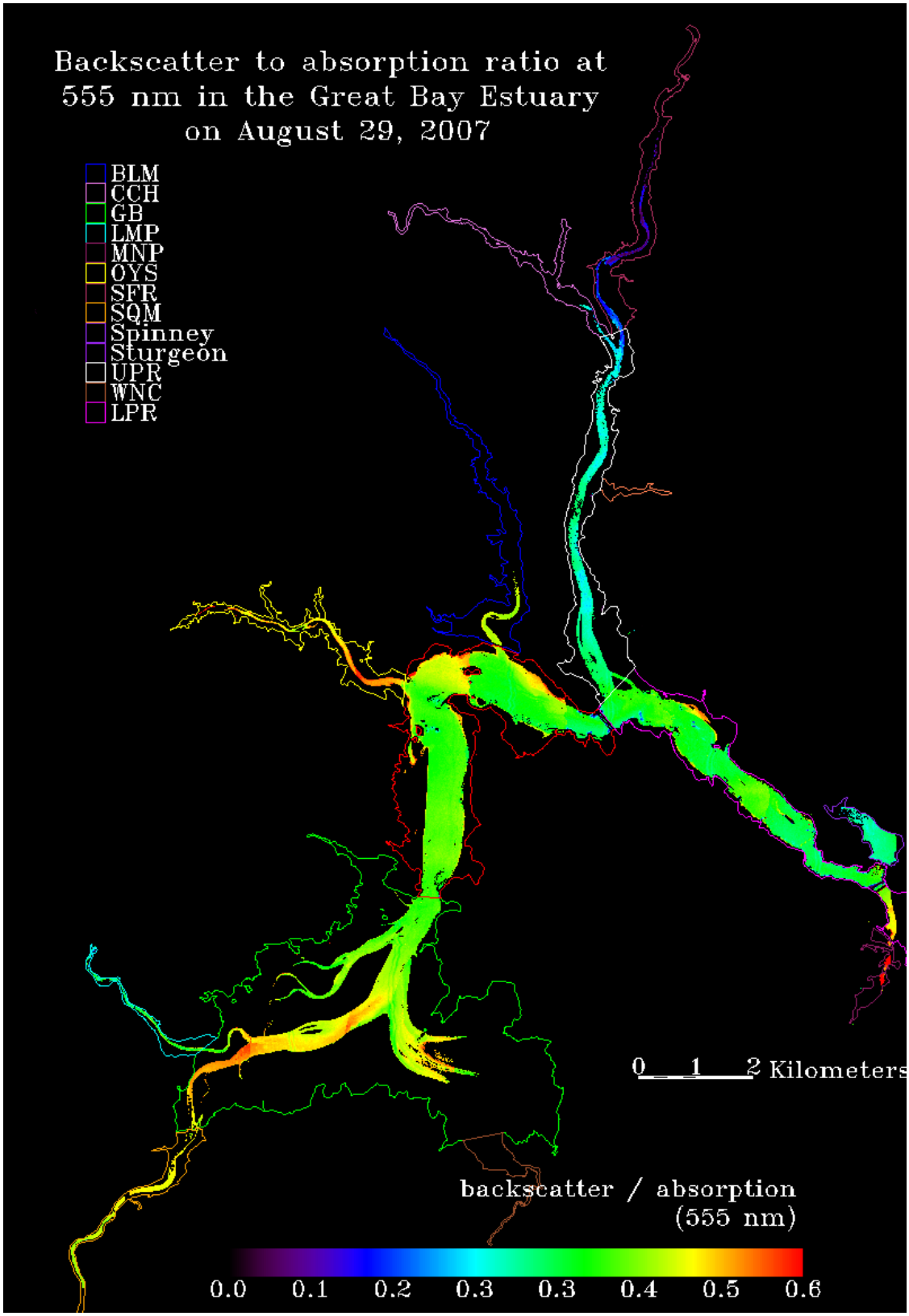

Figure 8.20 Remotely sensed ratio of optical backscatter and absorption at 555 nm for the Great Bay Estuary on august 29, 2007. Outlines of the NHEP estuarine assessment zones are given.

8.2.5 Comparison of Spatial estimates of the water Quality

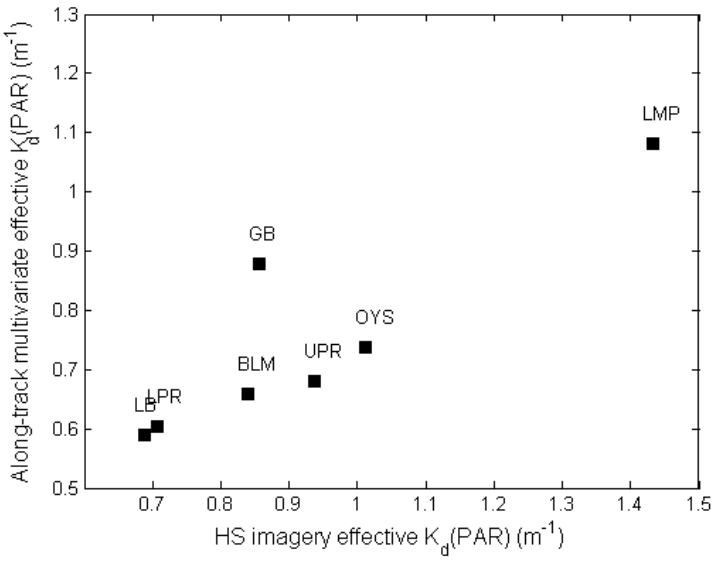

Figure 8.21 Comparison of HS imagery and along-track estimates of the effective K_d(PAR) for August 29. There was good agreement for the mean observed values in six of the seven NHEP assessment zones with 96% of the variability of one explained by the other. The GB multivariate derived mean was higher than that derived from HS imagery.

On August 29 there were three sources of high spatial resolution estimates of the effective diffuse attenuation coefficient for PAR, K_d(PAR): 1) the HS imagery, 2) the along-track multivariate model, and 3) the along-track ac-9 estimate. Mean K_d(PAR) values from each of the NHEP assessment zones estimated with the HS imagery and the along-track multivariate model agreed well explaining 77% of the variability of one by the other (Figure 8.21). The along-track estimate for the Great Bay area was greater that from the HS imagery. Under sampling of waters of greater water clarity with the along track measurements and or temporal variability may explain this difference. The decreased boat speed necessary for navigation in the more opaque waters of the western portion of the Great Bay including those of leading towards the Lamprey and Squamscott Rivers may have lead to a relative increase in the number of observations in these waters. Excluding GB from the comparison of the two estimates increased the variability in the along-track multivariate K_d(PAR) explained by that from the HS imagery to 96.5% (slope = 0.66 (±0.06), intercept = 0.11 (± 0.06), F=110, p<0.01).

8.3 Eelgrass survival depth

The PAR attenuation coefficient from the buoy measurements and the HS imagery was used to calculate investigate the temporal and spatial variability in the eelgrass survival depth. This was calculated based on the assumption that survivability can be related to the fraction of surface irradiance available to eelgrass which is a function of depth and the diffuse attenuation coefficient (see Equation 5.1). Here we use the 22% surface light threshold as described in Koch (2001). Rearranging Equation 5.1 for a survival depth of 22% of surface light gives,

$$z_{survive} = \frac{\ln(22/100)}{K_d(PAR)} \qquad (8.4)$$

From the 2482 K_d(PAR) observations at the buoy the mean survival depth was 1.47 m with a standard deviation of 0.58 m (Figure 8.22).

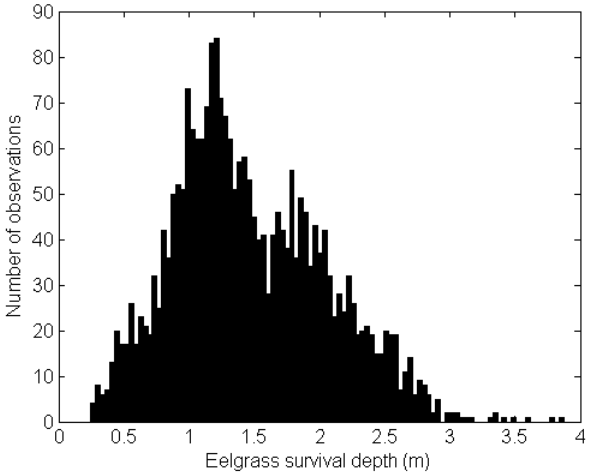

Figure 8.22 Relative frequency of eelgrass survival depths determined from K_d(PAR) measured with the Great Bay Coastal Buoy. The mean depth was 1.47 m. At the time of the collection of the HS imagery on August 29 the calculated survival depth was 1.66 m corresponding to a K_d(PAR) of 0.91 m^{-1}.

The 22% surface light level eelgrass survival depth was also calculated from the K_d(PAR) derived from HS imagery. These survival depths are the depth below the mean water level and depths less than one meter effectively indicating no eelgrass possible as they would be associated with intertidal areas. A value of downwelling distribution function (Do) determined with buoy measurements of 1.29 was used to convert the 'effective' attenuation measurements retrieved from the HS imagery to in situ K_d(PAR). The HS derived survival depth at the Great Bay Coastal buoy of 1.64 m agreed well with that determined in situ of 1.66 m reflecting the proximity of the two K_d(PAR) estimates. Throughout the estuary survival depth estimates ranged from 0.38 m in areas of Great Bay and the Oyster river to 2.33 m in the Lower Piscataqua River (Table 8.5 and Figure 8.23).

Table 8.5 Eelgrass survival depth estimates from the HS imagery for each of the observed NHEP assessment zones.

Assessment		22% Survival Depth			
Zone	Num	Min	Max	Mean	Stdev
BLM	282872	1.068	1.679	1.404	0.100
CCH	114945	0.625	1.063	0.911	0.056
GB	2729484	0.376	2.072	1.457	0.319
LB	1181525	0.406	2.162	1.720	0.149
LMP	70600	0.508	1.084	0.833	0.106
LPR	695926	0.511	2.325	1.685	0.182
NMP	50993	0.962	1.578	1.235	0.134
OYS	208838	0.375	1.978	1.244	0.308
SFR	236631	0.219	1.171	0.899	0.129
SQM	116069	0.437	0.927	0.659	0.044
Spinney	82745	0.962	1.350	1.094	0.069
UPR	526272	0.598	1.956	1.287	0.216

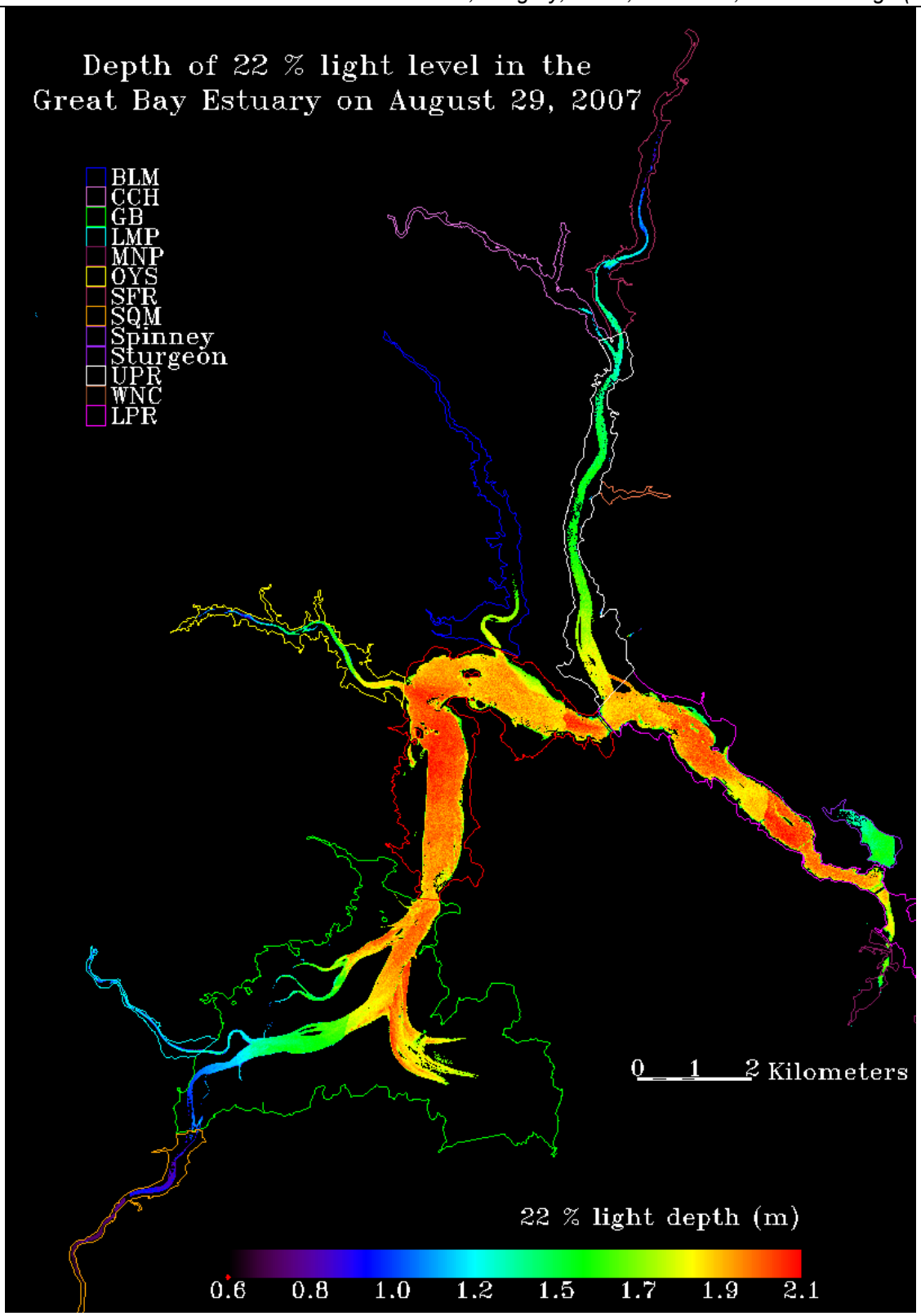

Figure 8.23 Spatial distribution of eelgrass survival depth assuming that greater than 22 % of surface irradiance is necessary determined with HS imagery on August 29, 2007. These survival depths are the depth below the mean water level and depths less than one meter effectively indicating no eelgrass possible as they would be associated with intertidal areas.

9 Conclusions

The variability of light attenuation in the Great Bay Estuary was assessed in three ways during 2007. Time-series measurements at a single location, that of the Great Bay Coastal Buoy, allowed the temporal variability to be assessed. K_d(PAR) measurements were significantly correlated (r^2>0.95) to the concentrations of colored dissolved organic matter (CDOM), phytoplankton as indicated by chlorophyll-a, and non-algal particles derived from turbidity measurements. Specific attenuation coefficients for each of these optically important constituents derived with multiple linear regression indicated that daily mean contributions of non-algal particles and CDOM to the total attenuation were of a similar magnitude around 30%. The contribution of phytoplankton was less comprising on the order of 15 % of the total. Attenuation of water estimated by this approach was some 60% higher than that observed in some of the clearest natural waters (Morel et al. 2007) but of a similar magnitude to previous results using the same technique (Gallegos 2001). The contribution of water at the higher values obtained in this study suggested that the contribution of water to the mean daily attenuation was the same order of magnitude as the CDOM and non-algal particles. However, this may overestimate the contribution of water.

On August 29 and October 17 the collection of hyperspectral aerial imagery and in situ measurements, both from a continuous along-track system and from discrete grab samples, allowed the spatial variability in water clarity to be investigated. Problems with the calibration of the HS system meant that information below 555 nm was not used in the analysis which complicated the separation of the optically important constituents from the HS imagery. A novel technique for estimating water turbidity and K_d(PAR) from the available HS wavelengths in optically deep waters was developed. However, in all spatial data concentrations of the optically important constituents generally showed lower values towards the mouth of the estuary and higher values in the tributaries. Values of K_d(PAR) determined from light profiles, the along-track measurements with the multivariate model developed with buoy observations, and the those from the HS imagery on August 29 agreed well. Currently, the HS information collected on October 17 has not been processed due to time constraints.

The high degree of correlation between HS derived K_d(PAR) and those determined from the in situ measurements allowed eelgrass survival depth to be estimate for the deep waters over the majority of the Great Bay Estuary. This was based on the assumption that eelgrass need 22% of surface incident light to survive (Koch 2001). The 22% light survival depth was also estimated from the buoy observations and indicated that on August 29 the optical conditions were close to the average observed in 2007. These results suggest that the water clarity in Great Bay, Little Bay, and the Lower Piscataqua River was sufficient for eelgrass growth. The virtual absence of eelgrass from all but Great Bay suggests that other processes apart from light restricted growth are important for limiting eelgrass survival.

10 Recommendations (for future work or management strategies)

This work together with associated work on the spatial distributions of eelgrass and macroalgae in the Great Bay Estuary has highlighted the potential of HS aerial imagery for management of coastal waters. However, determination of water clarity was limited to optically deep water due to the complexities associated with the inclusion of remotely detectable bottom reflection. Various algorithmic approaches exist that can accommodate these optically more complex conditions but generally rely on wavelengths less than those available in this study.

Uncertainties associated with water depth and the inversion of the HS imagery could be further decreased if concurrent HS imagery and LIDAR information can be fused together. Such data has already been collected for the mouth of the Great Bay Estuary / Portsmouth Harbor where further eelgrass beds exist. This data could provide valuable information of future techniques for remote sensing of water quality and benthic habitat characteristics.

10.1 Table 11.1 Buoy instrumentation

Instrument	Variables	Units	Antifouling	Notes
Weatherpak 2000 (Coastal Environmental Inc.)	Air temperature Wind speed Wind direction Wind gusts Relative Humidity Barometric pressure GPS position	ºC m / s º m / s % mbar	None	All in one unit with one digital data out.
SBE37 SIP (Seabird Inc.)	Water temperature Conductivity Pressure (Depth) Salinity (calculated from above)	ºC S/m dbar psu	Tributyl tin plugs at inlet and outlet.	Pumped instrument. Pump failure can cause data quality to deteriorate.
ISUS (Satlantic Inc.)	Nitrate	µmol / L	Copper screen surrounding probe.	Optical instrument using UV absorption. Sediment in copper screen can cause fouling.
Cycle-PO4 (WetLABS Inc.)	Phosphate	µmol / L	Intake filter	Microfluidic wet chemistry reactions. Beta test instruments not available yet in real time. Limited success but getting better.
FLNTUS (WetLABS Inc.)	Chlorophyll-a (fluorometer) Turbidity Optical backscatter (700nm)	mg / m^3 NTU 1 / m	Copper faceplate and shutter with rubber wiper	Chlorophyll-a from fluorescence. Turbidity and backscatter from same sensor
FLCDS (WetLABS Inc.)	Colored dissolved organic matter (CDOM)	QSE ppb	Copper faceplate and shutter with rubber wiper	Fluorescence estimate calibrated with quinine Sulphate
Optode (Aanderaa Instruments Inc.)	Oxygen Percent saturation	µmol / L %	Wrapped in copper foil since 2005/08/28	Overgrowth of benthos (bryozoans) problematic before copper foil
Hyper OCR-I (Satlantic Inc.)	Downwelling irradiance (350-800 nm) at 1.10 m	µW cm^{-2} s^{-1} nm^{-1}	Copper shutter	Still prone to fouling under shutter. Sensor head acts as cup for sediment. PAR calculated by integrating between 400 & 700 nm.
AWAC (Nortek)	Current profile Bottom water temperature Wave properties	ms^{-1}	None	ADCP mounted on bottom to NE of buoy. Umbilical cable for telemetry.
Hyper OCR-I	Downwelling irradiance at the surface (300-800 nm)	µW cm^{-2} s^{-1} nm^{-1}	Spikes to prevent seagulls sitting on it.	See note on PAR above. Only deployed 2007/04/04
Hyper OCR-R	Upwelling radiance at 1.45 m (300-800 nm)	µW $cm^{-2}sr^{-1}$ s^{-1} nm^{-1}	Copper shutter	See note on PAR above. Only deployed 2007/04/04

10.2 Quality evaluation of the hyperspectral data set.

10.2.1 Introduction

A quality assurance (QA) of the hyperspectral (ASIA) data was done in order to evaluate the AISA dataset. Good QA results would allow processing the data "as is" and bad QA results would require pre-processing procedures or considering a different approach to process the data (instead of processing the data in the reflectance level). The reflectance data inside the water body was problematic for this specific study. There was no spectral information above 900 nm (i.e. the values were the same for all channels between 902 nm and 951 nm, Figure 10.1). In addition, the spectral signatures do not correlate with those of characteristic of estuarine environments available from an historical spectral library or measurements using a field spectrometer.

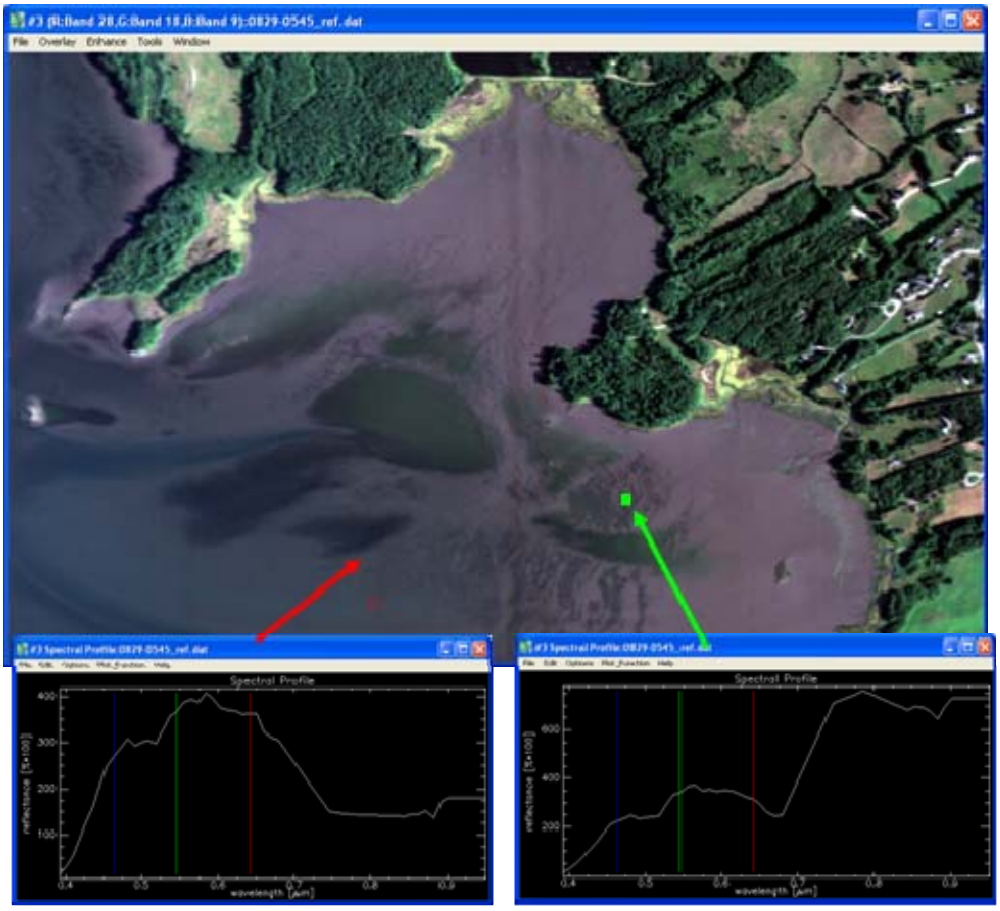

Figure 11.1 Two spectral-signatures bottom two panels from a reflectance-level image with image details in top panel (0829-0545 is the flight line). The spectral signatures on the bottom left (red box in the overview image) is a sandy exposed bottom and spectral signatures on the bottom right (green box in the overview image) is a vegetated bottom

Following these results, an evaluation was conducted on the imagery at a radiance level. The evaluation was conducted in two independent methods: simulated atmospheric model independent from the dataset (MODO) and simulated atmospheric model based on the hyperspectral dataset (TAFKAA). Oxygen mapping test was also conducted on the dataset.

10.2.2 MODO simulation

The MODO (MODTRAN4 Interface) simulation software is used in this study to simulate spectral signatures at a radiance level. The inputs provided are the environmental conditions (sample location, time, and atmospheric condition) and an end-member of interest. The goal of the MODO processing is to produce an independent signature dataset that can indicate the quality of the AISA data.

The methodology used in the MODO simulation was: field measurement of reference targets, simulate synthetic-spectral signatures from the targets collected in the field measurements, and compare between the synthetic-spectral signatures and the signatures from the radiance datasets. These steps are elaborated as follows:

1. Spectral signatures (reflectance) of different targets were collected. The signatures were mainly, sand, gravel, concrete, old (fair colored) asphalt, and new (dark) asphalt (Table 11.2). All signatures were collected around Great Bay (4.3.2008). Asphalt and concrete target are can be considered as ideal QA targets, since their spectral signature does not vary much with time (over a period of months) and can be considered stable.

Table 11.2 Summary table of the spectral signatures collected for the study

Target number	**Location**	**Target measured**
Target 1	Dover DMV Parking Lot	Asphalt
Target 2	Newick's Parking Lot	Asphalt Sand Concrete
Target 3	Hilton Park	Gravel Asphalt
Target 4	Northwest Scammel Bridge	Asphalt
Target 5	Durham's New Landing	Sand
Target 6	Durham's Old Landing	Sand
Target 7	Adam's Point	Asphalt
Target 8	New Market's Municipal Parking Lot	Gravel Asphalt

2. Spectral signatures (reflectance) of the different targets were imported into the software.

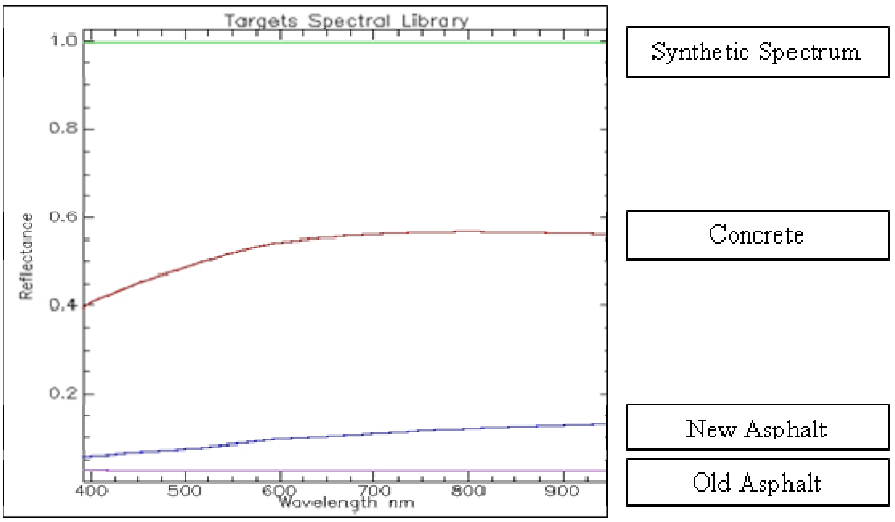

Figure 11.2 Spectral plot reflectance (value of 1 is 100 %) as a function of wavelength of the collected field measurement signatures and of the synthetic spectrum (white reference).

3. The sun geometry was calculated for the time of the HS survey (morning time) and was also calculated at evening for observing spectral changes.

4. The atmospheric conditions at the time of the survey were simulated.

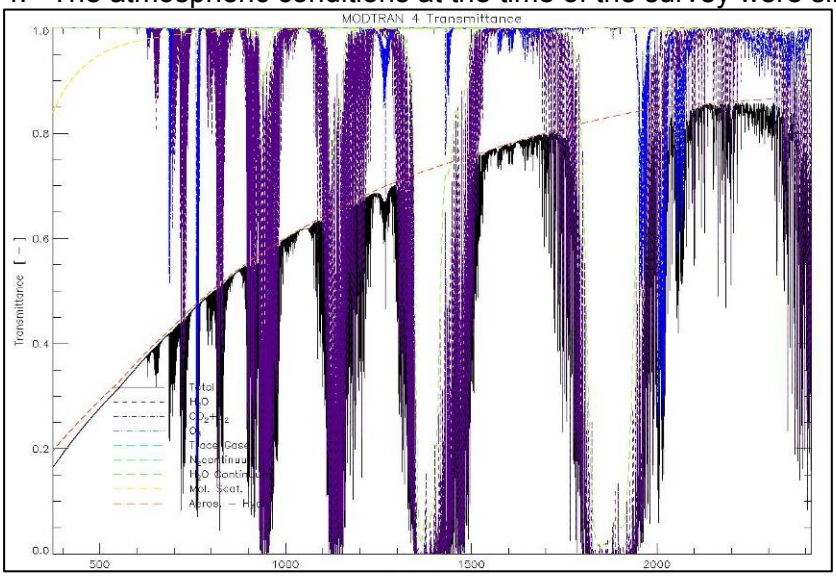

Figure 11.3 Spectral plot of the atmosphere in the transmittance level (transmittance value [%] as a function of wavelength [nm]) at the time of the survey. The black line in the plot represents the atmospheric transmittance.

5. The sensor's radiation as a function of wavelength was simulated based on the atmospheric conditions. The resulting product was a radiance plot (radiance value [$W/m^2sr \cdot nm$] as a function of wavelength [nm]) that can translate the field measurements to radiance values at the time of the survey.

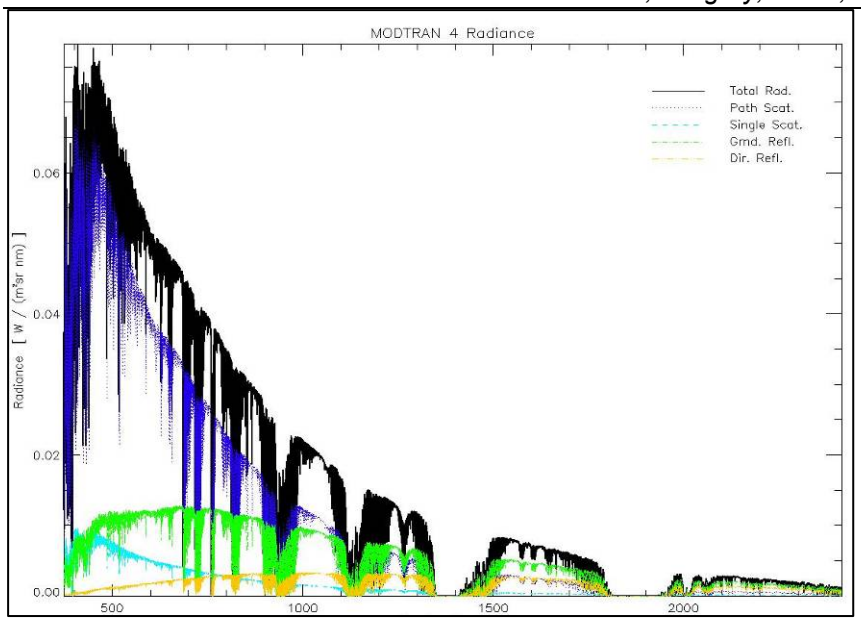

Figure 11.4 The radiance plot (radiance value [W/m^{2}sr·nm] as a function of wavelength [nm]). The black line represents the total radiance.

6. Radiance values for the different targets as a function of wavelength were simulated for morning time at 8:30 local time (blue spectrum) and for the afternoon time at 15:30 local time (red spectrum).

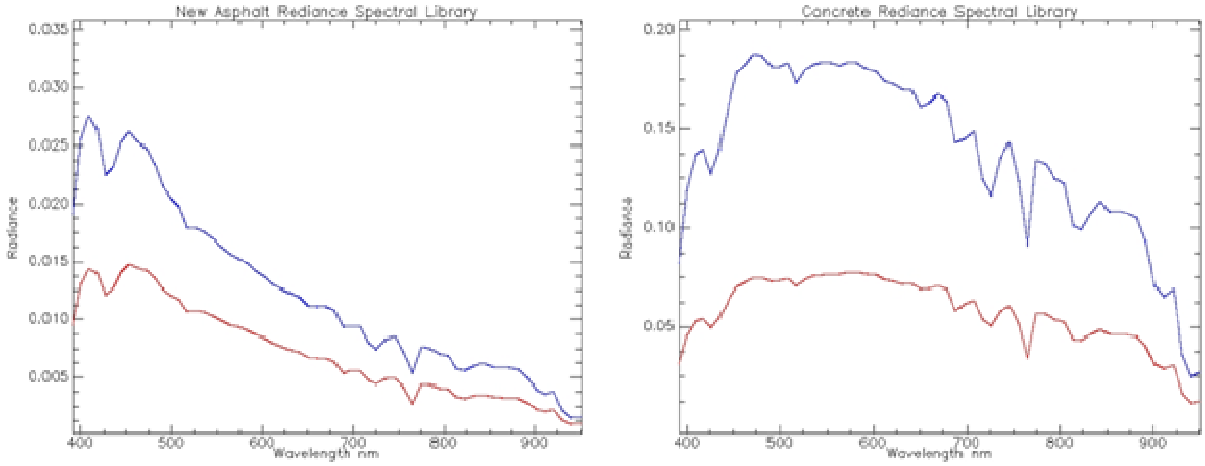

Figure 11.5 Simulated-spectral signatures in radiance [W/m^{2}sr·nm] of two targets measured in the field: new asphalt (left plot) and concrete (right plot). The blue line and the red line are the spectral signatures in radiance level for a morning survey (8:30 local time) and an afternoon survey, respectively.

7. The most prominent results were observed in the comparison of asphalt where a gain value in the blue to green-blue (400 nm to 550 nm) is noticed. The spectral signitured were compared in the radiance level and were also compared after a continuum removal normalization of the radiance values.

A

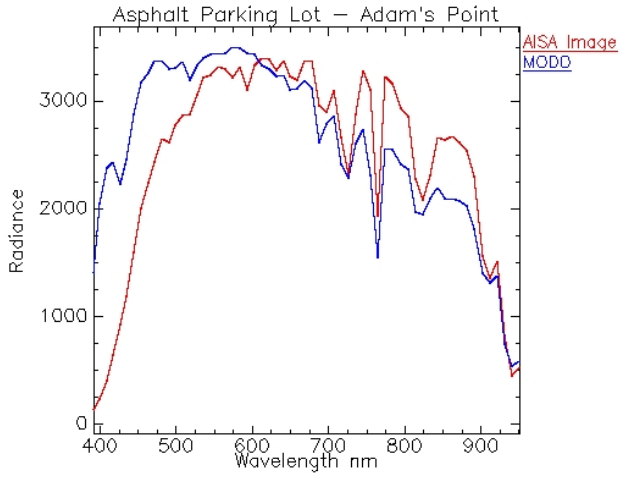

B

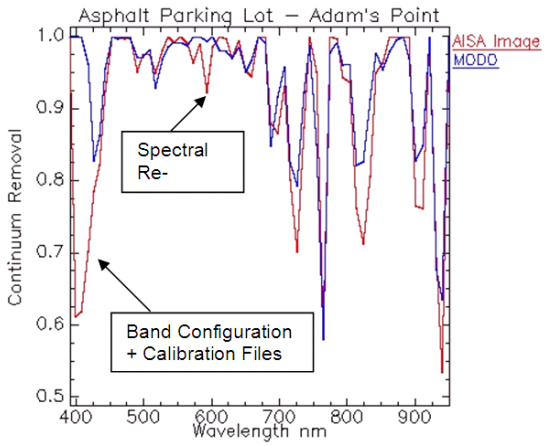

Figure 11.6 Spectral comparison of an asphalt target (Adam's Point). A) Comparison in the radiance level. B) Comaprison after a continuum removal normalization of the radiance values. The blue and red lines represent the AISA image and the field measurement simulated by MODO, respectively.

The results from the MODO simulation showed a good correlation between the spectral signatures of targets sampled from the AISA image and the field measurements in the 570 nm - 800 nm region. The correlation is both on the spectral values and the location of various spectral features along the signature. The correlation of the two datasets in the 400 nm – 550 nm region did not show good correlation. A gain artifact is noticed that might be caused due to a problem in the band configuration or the calibration files. Also, some spectral features vary between the two data sets. This might be due to a spectral re-sampling.

10.2.3 TAFKAA Atmospheric Correction of SPEC-TIR AISA/Eagle over-flight 08/29/2007

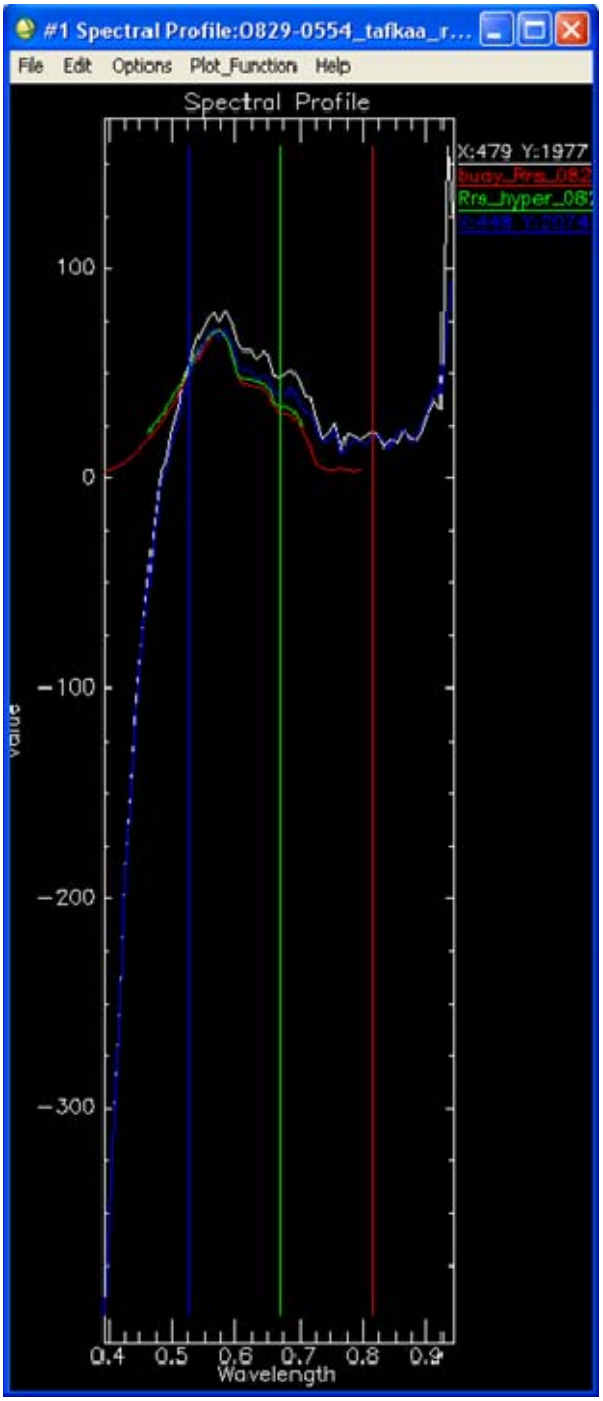

Figure 11.7 Remote sensing reflectance (R_{rs} * 10000) with wavelength. Tafkaa retrieved values (white line) and in-water measurements (red – buoy, green – profiling radiometer). The blue line is a nearby pixel.

The example is for a smaller subset of the main over-flight line that passed overhead of the buoy in Great Bay, NH. The calculated atmospheric correction corrected remote sensing reflectances from the HS over-flight (white and blue lines) are compared to those calculated at the buoy with in-situ sensors with hyperspectral sensors (HyperOCR, Satlantic Inc). These included sensors on the buoy (redline on Figure 11.7, surface E_s as well as an L_u and E_d pair at ~1m) as well as a submersible profiling radiometer (Hyperpro-II, green line).

The atmospheric correction was performed with Tafkaa – 6S with fixed values for atmospheric components over the whole scene. Tafkaa input files are provided below. Data sources for these values were:
Column ozone (289 DU) from NASA Ozone processing team (TOMS). Water vapor (2.3 cm) and aerosol properties (aerosol optical thickness was 0.17) were from the Aeronet processed Thompson farm Cimel Sun photometer.
Other atmospheric gasses were left as default including the NO2 which has a column value of 5e15 molecules.

Results: There appears to be good agreement with the spectra above ~ 0.55 µm (550 nm) but below this the HS imagery reflectances (and water leaving radiances) diverge significantly. Three possible causes for this disagreement at lower wavelengths include:

1) Overcorrection for aerosols,
2) High NO_2 concentrations with its associated increase in absorption at wavelengths below 600 nm (high NO_2 is associated with atmospheric pollution), or
3) Problems associated with instrument performance / calibration issues at these blue wavelengths.

Three additional Tafkaa runs were performed

to assess the possible contribution of the first aerosol overcorrection and NO_2 pollution: 1) For aerosol overcorrection the aerosol optical depth was set to zero such that no aerosol correction would be performed (Figure 11.8A). 2) For NO2 pollution the background concentration was increased by a factor of 90. NO_y data from the UNH AIRMAP facility at Thompson Farm indicated that there was a potential pollution event at the time (Figure 11.8B). 3) To assess the combined potential impact of the aerosol over correction and NO_2 pollution the aerosol optical depth was set to zero and NO_2 increased by a factor of 90 (Figure 11.8C). For all three additional atmospheric correction scenarios negative remote sensing reflectances were retrieved.

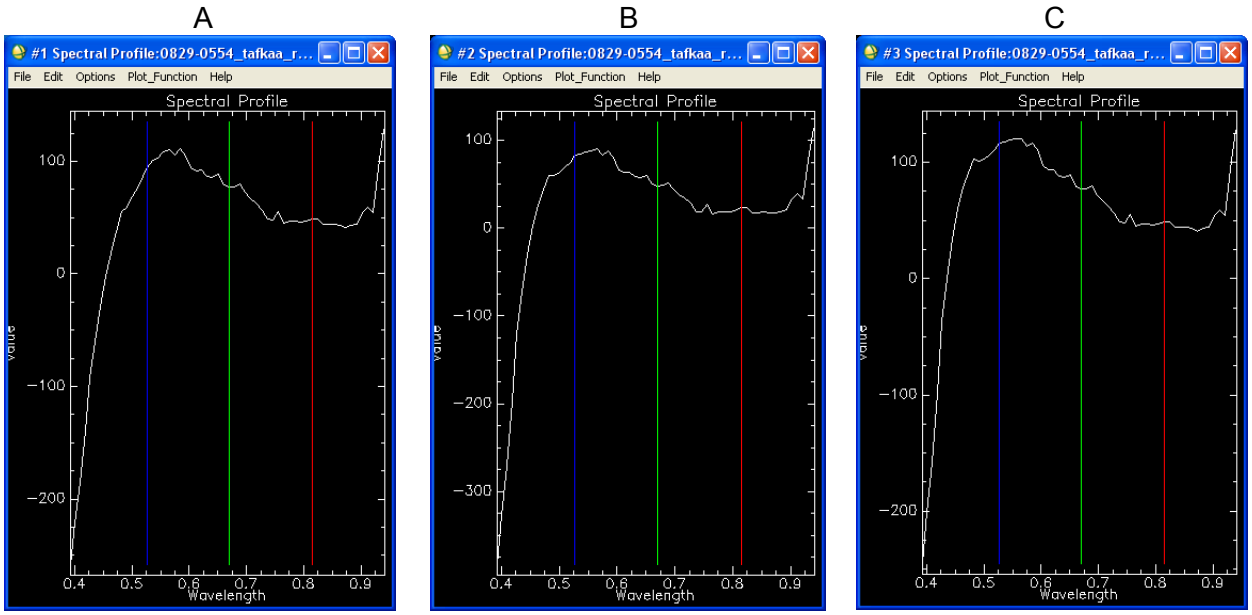

Figure 11.8 Remote sensing reflectances retrieved from three atmospheric correction scenarios. A) No aerosol correction, B) increased NO_2 by a factor of 90, and C) a combination of the other two.

10.2.4 Oxygen mapping

Oxygen (O_2) is well mixed gas in the atmosphere. The oxygen absorption is in 765 nm and can be used as a good indicator for several radiometric calibration issues. A shift in location between the MODO-simulated oxygen absorption and the hyperspectral dataset would indicate if there is a problem with the hyperspectral data. Results from the AISA dataset show that the there is a good match between the two absorption locations.

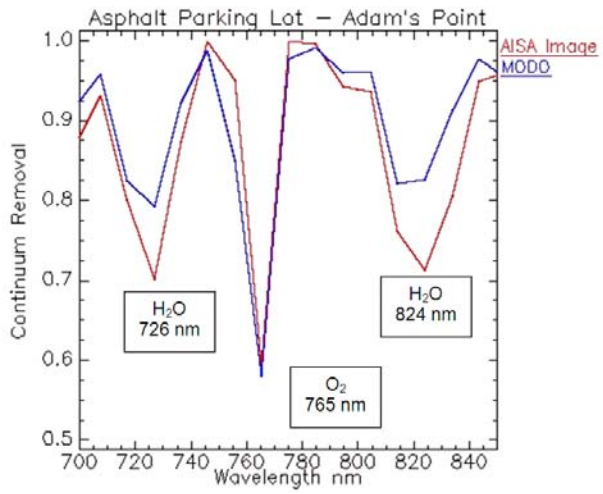

Figure 11.9 Spectral comparison of an oxygenabsorption (Adam's Point) after a continuum removal normalization of the radiance values. The blue and red lines represent the AISA image and the field measurement simulated by MODO, respectively. In addition to the oxygen absorption (765 nm) the water (H_2O) absorption (726 nm and 824 nm) is also noticed.

10.2.5 QA summary

The evaluation of the hyperspectral dataset was conducted in two independent methods: simulated atmospheric model independent from the dataset (MODO) and simulated atmospheric model based on the hyperspectral dataset (TAFKAA). Oxygen mapping test was also conducted on the dataset. Both methods showed AISA spectra above 0.55 µm (550 nm). The AISA imagery reflectance below 0.55 µm diverges significantly from both the comparison methods.

These results were indicative of problems associated with instrumentation and not the atmospheric correction at these blue wavelengths. To verify the approach taken we consulted with Marcos Montes of the Naval Research Laboratory who is the research physicist responsible for the current development of the Tafkaa atmospheric correction software. He agreed that this issue was probably an instrument/calibration/processing problem. This conclusion was shared by Oliver Weatherbee of SpecTIR and appears to be due to problems associated with their calibration source for the instrument and its traceability to NIST. SpecTIR are working to fix this problem but at the time of writing this report no solution was available.

The approach taken in order to continue with the study was to re-process the radiance level dataset and convert it to a reflectance dataset using TAFKAA. The spectral information below 0.55 µm cannot be used. According to data provided, the processing and analysis for the study focused only the spectral range above 0.55 µm.

10.3 Additional data tables

10.3.1 Continuous along-track sampling

Table 11.3 Water quality parameters for NHEP Assessment zones for August 29, 2007.

Zone	Parameter	Units	Number	Min	10th %	Median	Mean	90th %	Max
BLM	Water Temperature	ºC	1532	20.00	20.19	20.71	20.68	21.11	21.43
	Salinity	psu	1532	28.24	28.86	29.46	29.31	29.61	29.65
	Chl-a	(mg/m^3)	1532	10.55	10.92	12.05	12.92	16.04	17.47
	CDOM	ppbQSE	1532	4.15	5.01	5.86	5.87	6.75	7.28
	c(660)	m^{-1}	1532	2.03	2.52	3.41	3.40	4.20	5.63
	c(650) ac-9	m^{-1}	1011	1.62	2.12	3.08	2.99	3.83	4.22
GB	Water Temperature	ºC	5892	21.35	22.01	22.39	22.35	22.67	23.06
	Salinity	psu	5892	22.58	26.76	29.04	28.43	29.26	29.43
	Chl-a	(mg/m^3)	5892	13.25	14.53	18.52	19.71	26.66	36.78
	CDOM	ppbQSE	5892	5.18	6.26	9.63	11.58	17.35	41.73
	c(660)	m^{-1}	5892	1.84	2.49	3.84	4.96	9.36	13.31
	c(650) ac-9	m^{-1}	5885	1.57	2.25	4.19	4.91	9.68	12.36
LB	Water Temperature	ºC	3881	17.34	18.79	21.37	20.75	21.71	21.87
	Salinity	psu	3881	29.09	29.31	29.43	29.51	29.87	30.22
	Chl-a	(mg/m^3)	3881	7.68	9.40	12.05	11.83	13.40	14.80
	CDOM	ppbQSE	3881	4.06	4.61	5.46	5.50	6.07	10.83
	c(660)	m^{-1}	3881	1.65	2.04	2.42	2.62	3.71	5.59
	c(650) ac-9	m^{-1}	2096	1.25	1.68	1.99	2.08	2.61	3.99
LMP	Water Temperature	ºC	786	21.92	22.28	22.73	22.65	22.91	23.04
	Salinity	psu	786	17.68	19.85	21.74	21.33	22.63	23.23
	Chl-a	(mg/m^3)	786	22.96	23.49	26.96	29.28	37.12	37.57
	CDOM	ppbQSE	786	15.86	24.31	33.81	32.50	38.09	45.32
	c(660)	m^{-1}	786	4.02	4.08	4.47	4.55	5.06	6.70
	c(650) ac-9	m^{-1}	786	4.16	4.25	6.21	6.27	7.95	8.17
LPR	Water Temperature	ºC	686	16.30	16.35	17.23	17.14	17.90	18.76
	Salinity	psu	686	29.88	30.10	30.27	30.28	30.48	30.53
	Chl-a	(mg/m^3)	686	6.48	6.55	7.53	7.45	8.36	9.26
	CDOM	ppbQSE	686	3.54	3.71	3.98	4.09	4.59	4.94
	c(660)	m^{-1}	686	2.10	2.30	3.70	3.55	4.45	4.75
	c(650) ac-9	m^{-1}	345	1.68	1.87	2.44	2.57	3.35	3.52
OYS	Water Temperature	ºC	1030	20.70	20.88	21.46	21.35	21.64	21.75
	Salinity	psu	1030	28.50	28.72	28.93	29.04	29.50	29.52
	Chl-a	(mg/m^3)	1030	11.52	11.75	15.11	14.16	15.93	17.17
	CDOM	ppbQSE	1030	4.61	5.04	6.25	6.14	7.31	8.00

	c(660)	m^{-1}	1030	2.06	2.41	4.48	4.29	6.02	6.78
	c(650) ac-9	m^{-1}	1026	1.68	2.00	3.08	3.19	4.38	5.22
UPR	Water Temperature	C	1058	18.07	19.07	21.25	20.85	22.05	22.50
	Salinity	psu	1058	25.35	25.97	27.78	27.91	29.82	30.04
	Chl-a	(mg/m3)	1058	8.33	9.34	15.59	15.09	21.38	22.66
	CDOM	ppbQSE	1058	3.72	4.06	5.87	6.66	11.25	13.56
	c(660)	m-1	1058	1.81	2.07	3.25	3.32	4.65	5.83
	c(650) ac-9	m-1	401	1.45	1.78	2.93	3.01	4.23	4.93

Table 11.4 Water quality parameters for NHEP Assessment zones for October 17, 2007.

Zone	Parameter	Units	Number	Min	10th %	Median	Mean	90th %	Max
BLM	Water Temperature	ºC	2239	13.98	14.05	14.26	14.27	14.48	14.61
	Salinity	psu	2244	26.41	27.20	27.87	27.70	28.01	28.06
	Chl-a	(mg/m^3)	2281	2.39	2.59	2.94	3.06	3.84	5.38
	CDOM	ppbQSE	2281	16.57	16.87	17.31	17.87	19.63	23.16
GB	Water Temperature	ºC	12223	13.56	13.69	14.06	14.18	14.86	15.96
	Salinity	psu	12263	9.43	24.57	27.57	26.96	27.88	27.97
	Chl-a	(mg/m^3)	12346	2.09	4.02	6.30	6.32	8.98	11.59
	CDOM	ppbQSE	9174	16.19	18.12	20.21	22.30	29.13	78.42
LB	Water Temperature	ºC	9334	13.09	13.30	14.24	14.23	15.42	15.51
	Salinity	psu	9373	22.51	27.69	27.88	27.84	28.21	28.69
	Chl-a	(mg/m^3)	9454	2.80	3.59	4.88	5.35	8.44	10.52
	CDOM	ppbQSE	8778	16.01	16.73	17.35	18.08	19.90	33.42
LMP	Water Temperature	ºC	1256	15.18	15.57	16.20	16.10	16.60	16.81
	Salinity	psu	1247	6.34	6.68	10.71	13.18	22.45	25.87
	Chl-a	(mg/m^3)	1262	3.38	3.55	3.70	3.73	3.93	4.54
	CDOM	ppbQSE	1262	28.38	38.26	57.68	53.91	68.02	70.86
LPR	Water Temperature	ºC	2186	13.84	13.90	14.09	14.08	14.25	14.72
	Salinity	psu	2173	17.05	22.59	27.99	26.79	28.18	28.26
	Chl-a	(mg/m^3)	2191	2.67	2.82	3.09	3.10	3.34	4.51
	CDOM	ppbQSE	2191	16.62	16.87	17.33	19.08	20.20	39.30
UPR	Water Temperature	ºC	3302	13.77	13.94	14.08	14.12	14.36	14.66
	Salinity	psu	3290	9.44	9.82	12.28	12.73	16.20	21.96
	Chl-a	(mg/m^3)	3333	2.69	2.85	3.05	3.29	4.11	7.92
	CDOM	ppbQSE	3287	16.51	42.36	50.70	49.56	55.32	57.00

11 References

Gallegos, C. L. 2001. Calculating optical water quality targets to restore and protect submerged aquatic vegitation: overcoming problems in partitioning the diffse attenuation coefficient for photosynthetically active radiation. Estuaries **24:** 381-397.

Gao, B., M. J. Montes, Z. Ahmad, and C. O. Davis. 2000. Atmospheric correction algorithm for hyperspectral remote sensing of ocean color from space. Applied Optics **39:** 887-896.

Gordon, H. R. 1989. Can the Lambert-Beer law be applied to the diffuse attenuation coefficient of ocean water? Limnology and Oceanography [LIMNOL. OCEANOGR.] **34:** 1389-1409.

Gordon, H. R. and others 1988. A semianalytic radiance model of ocean color. Journal of Geophysical Research **93:** 10909-10924.

Gordon, H. R., and A. Y. Morel. 1983. Remote assessment of ocean color for interpretation of satellite visible imagery. A review. Springer-Verlag.

Ioccg [ed.]. 2000. Remote Sensing of Ocean Colour in Coastal, and other Optically-Complex waters. IOCCG.

Koch, E. M. 2001. Beyond light: Physical, geological, and geochemical parameters as possible submersed aquatic vegetation habitat requirements. Estuaries **24:** 1-17.

Lee, Z.-P., and K. L. Carder. 2005. Hyperspectral remote sensing, p. 181-204. *In* R. L. Miller, C. E. Del Castillo and B. A. MckEE [eds.], Remote sensing of coastal aquatic environments. Springer.

Lee, Z., K. L. Carder, R. F. Chen, and T. G. Peacock. 2001. Properties of the water column and bottom derived from Airborne Visible Infrared Imaging Spectrometer (AVIRIS) data. Journal of Geophysical Research-Oceans **106:** 11639-11651.

Lee, Z. P., K. L. Carder, and R. A. Arnone. 2002. Deriving inherent optical properties from water color: a multiband quasi-analytical algorithm for optically deep waters. Applied Optics **41:** 5755-5772.

Lee, Z. P., K. L. Carder, C. D. Mobley, R. G. Steward, and J. S. Patch. 1998. Hyperspectral remote sensing for shallow waters. I. A semianalytical model. Applied Optics **37:** 6329-6338.

---. 1999. Hyperspectral remote sensing for shallow waters: 2. Deriving bottom depths and water properties by optimization. Applied Optics **38:** 3831-3843.

Loisel, H., and A. Morel. 1998. Light scattering and chlorophyll concentration in case 1 waters: A reexamination. Limnology and Oceanography [Limnol. Oceanogr.] **43:** 847-858.

Mobley, C. D. 1994. Light and water: radiative transfer in natural waters. Academic Press, Inc.

Mobley, C. D. and others 2005. Interpretation of hyperspectral remote-sensing imagery by spectrum matching and look-up tables. Applied Optics **44:** 3576-3592.

Montes, M. J., B. Gao, and C. O. Davis. 2001. A new algorithm for atmospheric correction of hyperspectral remote sensing data., p. 23-30. *In* W. E. Roper [ed.], Geo-Spatial Image and Data Exploitation II. SPIE.

Morel, A. 1987. Chlorophyll-specific scattering coefficient of phytoplankton. A simplified theoretical approach. Deep-Sea Research [DEEP-SEA RES.] **34:** 1093-1105.

Morel, A., and D. Antoine. 1994. Heating rate within the upper ocean in relation to its bio-optical state. Journal of Physical Oceanography [J. PHYS. OCEANOGR.] **24:** 1652-1665.

Morel, A. and others 2007. Optical properties of the "clearest" natural waters. Limnology and Oceanography **52:** 217-229.

Morel, A., and S. Maritorena. 2001. Bio-optical properties of oceanic waters: A reappraisal. Journal of Geophysical Research. C. Oceans [J. Geophys. Res. (C Oceans)] **106:** 7163-7180.

Morrison, J. R. 2003. In situ determination of the quantum yield of phytoplankton chlorophyll *a* fluorescence: a simple algorithm, observations, and a model. Limnology and Oceanography **48:** 618-631.

Mueller, J. L., R. Bidigare, C. Trees, J. E. Dore, D. Karl, and L. Van Heukelem. 2003. Biogeochemical and Bio-Optical Measurements and Data Analysis Protocols. *In* J. L. Mueller, G. S. Fargion and C. McClain [eds.], Ocean Optics Protocols For Satellite Ocean Color Sensor Validation, Revision 4, Volume 5. NASA.

Pegau, W. S. and others 2003. Inherent Optical Properties: Instruments, Characterizations, Field Measurements and Data Analysis Protocols. *In* J. L. Mueller, G. S. Fargion and C. McClain [eds.], Ocean Optics Protocols For Satellite Ocean Color SensorValidation, Revision 4, Volume IV. NASA.

Preisendorfer, R. W., and C. D. Mobley. 1985. Unpolarized irradiance reflectances and glitter patterns of random capillary waves on lakes and seas, by Monte Carlo simulation, p. 141. NOAA Tech. Memo. ERL PM EL. Pacific Mar. Environ. Lab.

---. 1986. Albedos and glitter patterns of a wind-roughened sea surface. J. Phys. Ocean. **16:** 1293-1316.

Ricchiazzi, P., S. Yang, C. Gautier, and D. Sowle. 1998. SBDART: A research and teaching software tool for plane -parallel radiative transfer in the Earth's atmosphere. Bulletin of the American Meterological Society **79:** 2101-2114.

Sathyendranath, S., and T. Platt. 1988. The spectral irradiance field at the surface and in the interior of the ocean: A model for applications in oceanography and remote sensing. Journal of Geophysical Research. C. Oceans **93:** 9270-9280.

Smith, R. C., and K. S. Baker. 1978. The bio-optical state of ocean waters and remote sensing. Limnology and Oceanography **23:** 247-259.

Sosik, H. M. 2007. Characterizing seawater constituents from optical properties. *In* M. Babin, C. S. Roesler and J. J. Cullen [eds.]. Monographs on oceanographic methodology. UNESCO.

Strickland, J. D. H., and T. R. Parsons. 1972. A practical handbook of sea water analysis. Fisheries Research Board of Canada.

Ward, L. G., and F. L. Bub. 2005. Temporal variability in salinity, temperature and suspended sediments in a Gulf of Maine estuary (Great Bay Estuary, New Hampshire), p. 151-142. *In* D. M. FitzGerald and K. J. [eds.], High Resolution Morphodynamics and Sedimentary Evolution of Estuaries. Springer.